



Microseismic Monitoring of Laboratory Hydraulic Fracturing Experiments in Granitic Rocks for Different Fracture Propagation Regimes

A. Butt¹ · A. Hedayat¹ · O. Moradian¹

Received: 9 May 2023 / Accepted: 5 November 2023 / Published online: 9 December 2023
© The Author(s), under exclusive licence to Springer-Verlag GmbH Austria, part of Springer Nature 2023

Abstract

While hydraulic fracturing (HF) is a widely employed process, the underlying fracturing processes are still heavily contested. The attributes of the HF generated fracture network can exhibit substantial variation when dealing with specific HF propagation regimes encountered in the field. In this study, HF experiments were performed on true-triaxially loaded Barre granite cubes, with microseismic monitoring, to identify and characterize the fracturing mechanisms associated with different viscosity injection fluids. Utilizing fluids with high (oil/1450 cP) and low (water/1 cP) viscosity represented two key HF propagation regimes: viscosity- and toughness-dominated. The experiments conducted with oil involved higher breakdown pressures, larger fluid volumes, and slower fracture propagation speeds. The frequency–magnitude distribution (b value) for all experiments (1.9–2.3) was similar to those encountered for large-scale operations. Slightly larger b values were encountered during the initiation phase (2.4–2.7) relative to the fracture propagation and post-fracturing phases (1.9–2.2). Techniques such as polarity and moment-tensor inversion were utilized to characterize the source mechanisms. For the HF experiments with oil, tensile fractures were most dominant (92%) in the initiation phase compared to fracture propagation and post-fracturing phases (70–75%). Similar tensile fracturing dominance was not observed with water, attributable to fluid permeation and leak-off. Regardless of the injection fluid or classification criteria employed, tensile fractures were the dominant type consistently, with fewer occurring in water experiments but the specific ratio of crack types varied with different source mechanism criteria employed.

Highlights

- Evolution of fracturing processes and their source mechanisms during hydraulic fracturing of Barre granite with high and low viscosity fluids.
- Highlighting the dissimilarity between fracture source mechanisms using multiple classification criteria.
- The proportion of fracture mechanisms (tensile/shear/compression) varied significantly depending on the classification criteria employed.
- Tensile fractures were found to be dominant both for high and low viscosity injection experiments.
- High viscosity fluids resulted in a higher percentage of tensile fractures relative to low viscosity fluids.

Keywords Hydraulic fracturing · True triaxial loading · Granite · Fracture propagation regimes · Fracture source mechanisms

1 Introduction

Hydraulic stimulation techniques have been used over many decades to increase the permeability of sedimentary reservoir rocks for oil and gas production (Maxwell et al. 2009b; Warpinski 2009; Warpinski et al. 2012). In recent years,

✉ A. Butt
ambutt@mines.edu

¹ Department of Civil and Environmental Engineering,
Colorado School of Mines, Golden, CO, USA

the number of HF applications in hard crystalline rocks has increased considerably [e.g., enhanced geothermal systems (EGS)]. In EGS, HF is used to stimulate and increase the permeability of an unconventional reservoir for cost-effective heat extraction (Henley and Ellis 1983; Olasolo et al. 2016). Stimulation of these kilometer deep geothermal reservoirs in crystalline basements have induced large-magnitude seismic events (e.g., Basel, Switzerland (Herrmann et al. 2019) and Pohang, South Korea (Grigoli et al. 2018)) more frequently than oil and gas stimulation operations (McClure and Horne 2014a). Although significant research efforts have attempted to understand reservoir geomechanics in sedimentary rocks, less attention has been given to crystalline rocks. Consequently, understanding the evolution of HF initiation and propagation in crystalline granitic rocks, the underlying fracture mechanisms, and their relationship to different injection parameters is crucial for the successful implementation and overall optimization of deep underground stimulation operations in these rocks.

In the field, HF propagation transitions between specific fracturing states represented by various dominating propagation regimes involving different competing physical processes. For an impermeable material, HF propagation can occur in either the viscosity propagation regime (VPR) or toughness propagation regime (TPR), depending upon a variety of factors, such as the injection fluid properties (rate and viscosity), the properties of rocks, and the far field stresses (Sarmadivaleh 2012). If the energy consumed in the creation of new fracture surfaces is small relative to the viscous dissipation energy, VPR is the dominant regime. In the TPR, the energy spent on new fracture surface creation is much larger than the viscous counterpart (Detournay 2004). HF propagation in most field operations occurs in the VPR (Detournay 2016); however, with the recent increase in utilizing low-viscosity fluid (e.g., liquid or supercritical CO₂), the HF propagation regime could transition to TPR (Huang et al. 2019). Both the hydro-mechanical response and the fracture profiles can vary among fracture propagation regimes (Li et al. 2020), which means that understanding the characteristics of the generated HF for specific situations involving different propagation regimes is essential for efficient HF design.

The majority of past recorded seismic data from large and intermediate field-scale HF operations (mostly VPR) have pointed towards the dominance of shear fracturing (Gischig et al. 2018; Horálek et al. 2010; Maxwell 2011; Maxwell and Cipolla 2011). Some researchers (Jung 2013; McClure 2012; McClure and Horne 2014a,b) argued against the pure shear stimulation supposition for granitic rocks and instead proposed that HF propagation in granitic rocks contains a much higher percentage of new fracturing than previously thought and is actually a combination of both the tensile fractures and the shearing of pre-existing fractures.

Observations from a few large-scale EGS HF projects (Fenton Hill (Norbeck et al. 2018) and Sanford Underground Research Facility (Schoenball et al. 2020)) supported this notion of combined-type fracturing. Nevertheless, the primary mechanism governing the permeability evolution during stimulation remains a topic of contention within the scientific community.

Seismic monitoring, or acoustic emission (AE) monitoring at the laboratory scale, has been successfully used to monitor the initiation and propagation of laboratory HF in brittle rocks (Lockner 1993; Stanchits et al. 2014) with the following examples focusing on granite rock specimens (e.g., Solberg et al. 1980; Zhuang et al. 2019a, b; Hu et al. 2020). There are studies which have explicitly investigated the influence of injection parameters (injection fluid's rate and viscosity) on the source mechanisms of the generated seismicity. The selection of these injection parameters may dictate if the HF propagation regime is viscosity or toughness-dominated. Li and Einstein (2019) conducted laboratory HF experiments on relatively small Barre granite prismatic cubes (76 × 152 × 25 mm), with a pre-existing vertical flaw, utilizing low viscosity injection fluid (3.89 cP) at two different injection rates (1.14 and 23.4 ml/min). While the injection rates were about one order of magnitude different, both experiments were believed to follow the TPR. This is because an extremely high injection rate was required to fulfill the requirements of VPR. The range of injection rate which can be selected is constrained by the capabilities of the injection pumps, rendering some injection rate options unattainable. Comparably, fluid's viscosity can be adjusted across multiple orders of magnitude enabling the attainment of various propagation regimes. Ishida and Company (Inui et al. 2014; Ishida 2001; Ishida et al. 2004, 2012, 2016) performed HF experiments in true-triaxially loaded Kurokami-jima granite with different viscosity fluids (transmission oil with 80 cP, water with 1 cP, and ultra-low-viscosity CO₂ with 0.05 cP). The fracture source mechanisms of the recorded microseismicity were determined through the polarity analysis (following Zang et al. 1998). Decreasing the viscosity of the injection fluid caused a shift in the fracture mechanisms from tensile-dominated to shear-dominated, as observed in water injection experiments compared to HF experiments conducted with oil. On the contrary, Hampton et al. (2013) hydraulically fractured Colorado Rose granite with a high-viscosity oil and low-viscosity brine solution and their analysis of the microseismicity detected during HF did not reveal any impact of viscosity on the fracture mechanisms. In a more recent study by Tanaka et al. (2021), the fracture source mechanisms during laboratory HF in Kurokami-jima granite specimens showed no significant differences despite the varying viscosity of the fluids used, which ranged from 0.8 to 1000 cP. These two studies utilized simplified Moment tensor (MT) inversion method (suggested by Ohtsu 1995),

Table 1 Properties of Barre granite

Density	2.65 gm/cm ³	Nur and Simmons (1969)
Porosity	0.006	
Permeability	10 ⁻¹⁸ –10 ⁻¹⁹ m ²	Kranzz et al. 1979
Poisson's ratio (ν)	0.13	Sano et al. (1992) Selvadurai et al. (2005)
Unconfined compressive strength (UCS)	170–190 MPa	Miller (2008)
Tensile strength	10–15 MPa	Dai and Xia (2010) Li and Einstein (2019)
Mode-I fracture toughness (K_{IC})	1.14 MPa.(m) ^{1/2}	Nasseri et al. (2006 and 2008)
Modulus of elasticity (E)	60 GPa	Selvadurai et al. (2005) Shirole et al. (2020)

instead of polarity, to ascertain the fracture source mechanisms. None of the above-mentioned studies identified the dominant fracturing propagation regime; however, utilizing high- and low-viscosity injection fluids could be indicative of VPR and TPR, respectively (Bunger et al. 2005). There is a research need to better understand the underlying fracture mechanisms, including the source mechanisms and nature of cracks, associated with different fracture propagation regimes.

Controlled laboratory HF experiments, coupled with comprehensive monitoring, have the potential to yield insights that may remain elusive when conducting large-scale field operations. However, the primary factors controlling the HF behavior (confining stresses and injection fluid parameters) in laboratory experiments should be carefully selected to replicate the fracturing state (VPR or TPR) encountered during field simulation operations. The scientific contribution of this study lies in the examination of fracture source mechanisms, determined using distinct classification criteria, for the microseismicity generated during HF propagation dominated by viscosity and toughness regimes. This involved performing HF experiments in true-triaxially loaded Barre granite cubes with high- and low-viscosity fluids. Selection of these fluids (gear oil and water) with different viscosities (1450 cP and 1 cP) triggered the HF propagation to occur in the viscosity- and toughness-dominated propagation regimes, respectively. Real-time AE monitoring enabled us to observe and analyze the complete spatio-temporal evolution of the HF process and the underlying source mechanisms, from initiation until breakdown of the laboratory granite specimens. Various techniques, such as polarity and moment-tensor inversion, were adopted to classify and compare the fractures source mechanisms of the detected AE events. The study also included post-experiment micro-structural analysis, which enabled a comparison between the induced HF and the associated seismic response of the tested specimens under the viscosity and toughness propagation regimes using oil and water as the injection fluids. The results of this study are intended to enhance our understanding of the physical processes associated with

HF in crystalline granitic rocks and the underlying fracture mechanisms, which eventually can enhance control and optimization of hydraulic stimulation operations.

2 Experimental Setup and Methodology

2.1 Material and Borehole Installation

HF was investigated using Barre granite cubes (165 mm × 165 mm × 165 mm) which represents the typical reservoir rocks encountered in geothermal projects (Cornet et al. 2007; McClure and Horne 2014a; Xie et al. 2015). These medium-grained granite cubes, with mineral grain sizes between 0.25 and 3 mm, were all acquired from the same block extracted from the E. L. Smith quarry located in the city of Barre, Vermont, USA (Dai et al. 2013). Feldspar is the main constituent mineral (65% by volume), followed by quartz (25% by volume) and biotite (6% by volume) (Dai and Xia 2013; Xia et al. 2008). Like most granites, Barre granite has a clear anisotropy with three mutually perpendicular cleavages, with varying strengths and densities of micro-cracks and minerals. These planes of weaknesses can be identified by obtaining compressional (P-) wave velocities in all three directions. The ultrasonic waveforms were acquired at multiple points on each side of all the tested Barre granite cubic specimens before drilling the boreholes for the fluid injection experiments. The arrival time was determined manually for each acquired waveform and its wave velocity was calculated. The velocity was similar for all different specimens in specific directions and was found to be ~4500 m/s (highest), ~4000 m/s (intermediate), and ~3500 m/s (slowest), along the three planes (hardway, grain, and rift). The velocity values, determined for various cubes, were similar to those of previous studies involving Barre granite (Dai et al. 2013; Dai and Xia 2013; Sano et al. 1992). Barre granite is an extensively studied rock and has rich literature. Table 1 displays the key material properties of Barre granite.

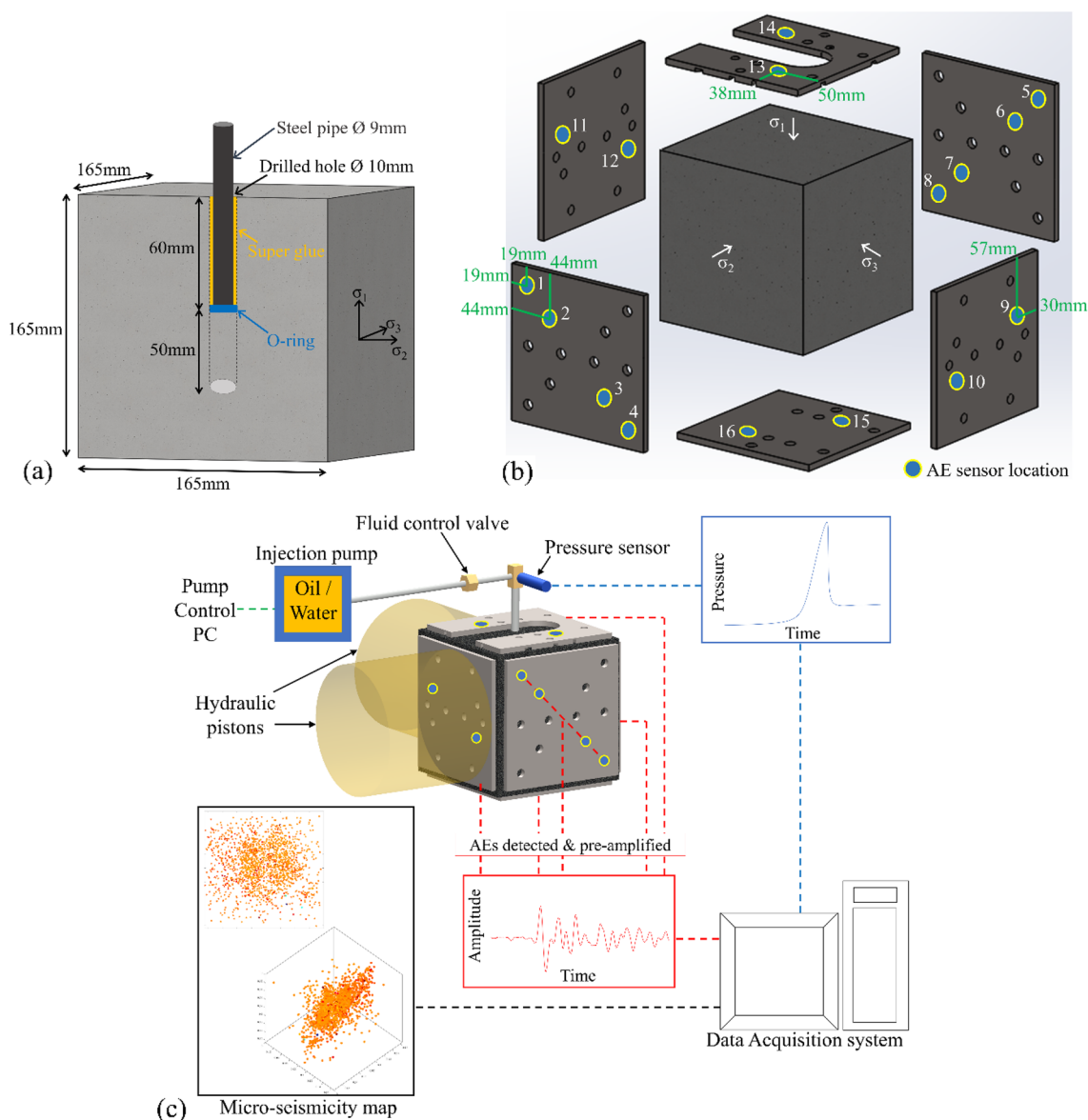


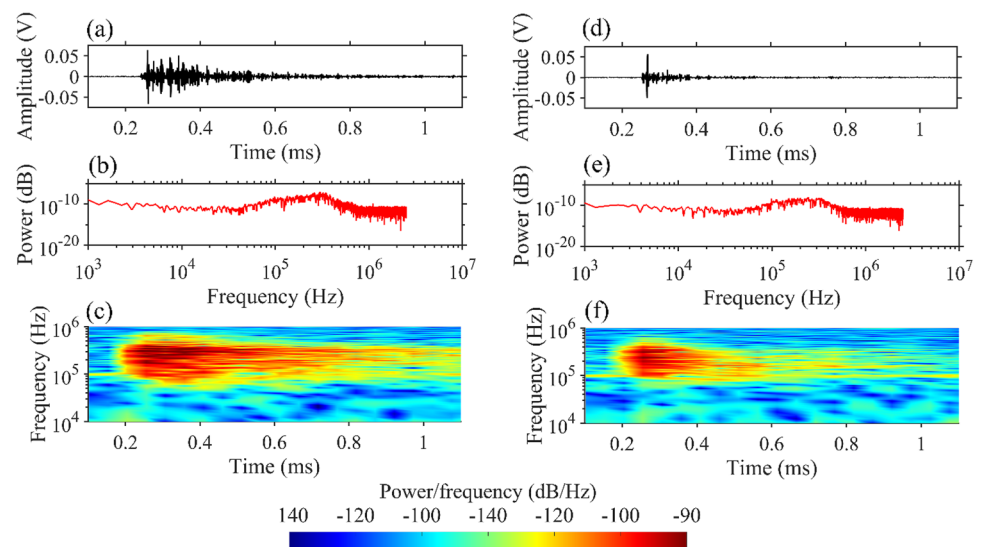
Fig. 1 **a** Schematic of the specimen and borehole configuration used for the HF experiments. A small borehole with a radius of 5 mm was drilled with respect to its distance to the boundaries of the cubic block (82.55 mm). **b** The location of 16 Nano-30 AE sensors in different platens, selected for the HF experiments providing sufficient coverage of the entire block. **c** Schematic of the complete

experimental setup. The data from the AE sensors were amplified and recorded in the computer for post-experiment analysis. The data from the hydraulic pistons and the pressure sensor, located 50 mm above the borehole entrance, were also recorded in the same computer to achieve synchronization between the pressure, confining stress, and the AE data (not to scale)

The rift plane was kept perpendicular to the σ_3 -direction for all experiments to encourage fracturing in the preferred orientation. A masonry drill bit was used to drill a 10 mm-diameter borehole parallel to the hard way plane up to a depth of 110 mm. Operating the drill press at slow speed ensured minimum damage in the vicinity of the borehole. A stainless-steel pipe with outer and inner diameters of 9 and 8 mm, respectively, was used to case the top 60 mm section of the borehole using high-strength epoxy. This arrangement provided an open HF section where the length

was 50 mm in the middle of the specimen (Fig. 1a). The importance of a well-oriented notch was emphasized by many past researchers, whereby the size and the direction of the initial notch affect how the HF initiates (Lhomme et al. 2005; Sarmadivaleh et al. 2013; Savic et al. 1993). However, slight deviations in the notch location with respect to the preferred fracture plane (perpendicular to σ_3) can result in fracture initiation from a point other than the pre-existing flaw (Fallahzadeh et al. 2017). Also, in the field, it is difficult to control the exact location and depth of the perforations

Fig. 2 Example of an AE waveform, power spectrum, and the spectrogram detected at BP for the **a–c** Oil_Test#1 and **d–f** Water_Test#1 HF experiments



and the damage induced by the drilling process may also govern the initiation of the fracture (Bunger and Lecampion 2017). Therefore, due to the uncertainty in obtaining a perfectly vertical notch at a certain depth inside the small borehole in hard Barre granite rock, the HF was performed without any initial notches. Instead, a high differential stress ($\sigma_2 - \sigma_3$) was used to assist the initiation and propagation of fracturing in the preferred direction. A high deviatoric stress ($\sigma_2/\sigma_3 = 2-3$) can result in a more planar and simpler HF geometry (Maxwell et al. 2016; Pan et al. 2020). Therefore, the maximum horizontal stress (σ_2) was chosen to be 2.5 times (8.625 MPa) the minimum horizontal stress (σ_3) (3.45 MPa). The vertical stress (σ_1) was kept at 17.25 MPa.

2.2 Experimental Setup

Three pairs of similar platens, for each loading direction, were designed to house the AE sensors (Fig. 1b). Each platen consisted of a 19 mm-thick rigid steel base plate (304 SS) with a high yield strength and a softer aluminum cover plate (6.35 mm). The positions of the sensors were selected based on the experimental setup and the number of available sensors, the expected location of the damage, and the optimum arrangement for AE detection. An additional cut-out in the top platen accommodated the injection assembly. Deformable spring-loaded washers were placed behind the sensors, which upon loading preserved continuous contact with the specimen surface. In addition, oven-baked honey (dehydrated in the oven at 100 °C for 90 min) was used to ensure proper coupling between the specimen and the sensors. This procedure has been successfully utilized in several acoustic studies (e.g., Hedayat et al. 2014).

The Teledyne ISCO 500HPx high-pressure syringe pump was used to inject fluid into the granitic rock. The injection pump had a volume capacity, flow range, and maximum

pressure limit of 507.38 ml, 1⁻⁶–408 ml/min, and 35 MPa, respectively. The highest viscosity fluid that could be accommodated in the injection pump was 1500 cP (mPa.s) and the pressure rating of the injection lines was 22.5 MPa. A true-triaxial frame with three independent hydraulic pistons was utilized for the loading of the blocks. The capacity of the two lateral and one vertical piston were 47 MPa and 62 MPa, respectively.

During the HF experiment, the emitted AE signals were detected and recorded using 16 piezoelectric sensors (Fig. 1b), at a sampling rate of 5 MHz, which were connected to two eight-channel boards from the MISTRAS group. These miniature Nano-30 sensors, with a small diameter of about 8 mm, had a relatively flat frequency response over the range of ~125–750 kHz. Hit-based triggering with a threshold of 50 decibels (dB) was used to manage the size of the collected AE data (i.e., the system recorded a signal upon registering any amplitude greater than 50 dB). To assist detection, the output voltage of the AE sensors was amplified by 20 dB using 2/4/6 PAC pre-amplifiers for all experiments. As an example, the single AE waveform along with the power spectrum and spectrogram recorded at BP is shown both for the oil (Fig. 2a–c) and water experiments (Fig. 2d–f). Perfect synchronization between the AE signals and the borehole pressure data was achieved by recording the pressure data directly in the AE system at a rate of 10 Hz. Figure 1c illustrates the schematic of the complete experimental setup.

The experimental protocol for all the experiments was as follows:

- After the specimen was placed in the true-triaxial setup, the stresses on the sides of the block were increased in the prearranged manner; the stresses on all three specimen sides were increased simultaneously to the σ_3

stress level. The stress in the σ_3 direction was kept constant, while the stresses in the σ_2 and σ_1 direction were increased to σ_2 . Ultimately σ_1 was then increased to the selected stress value.

- After tightening all the hydraulic system connections, a brief (5 min) constant pressure test was performed to identify any unlikely leakage in the complete system. Pressure was increased stepwise to ~ 7 MPa in ten steps of ~ 0.7 MPa for 30 s each. This value of injection pressure (7 MPa) was much lower than the expected value of breakdown pressure (BP) (the highest pressure recorded during an experiment) and, therefore, was not expected to cause any damage in the strong and relatively impermeable Barre granite block.
- After the important pre-check, the pressure in the borehole was reduced to 0.7 MPa, which served as the starting point for all the experiments, ensuring the saturation of the borehole and the injection lines. Fluid flow at a pre-selected constant rate (1 ml/min) from the injection pump commenced almost simultaneously with the activation of the AE data acquisition system.
- The fluid injection was continued after the BP of the specimen while acquiring AE data and the test was only stopped after the injection pressure appeared to be constant for a considerable period and without any substantial AE activity (less than 2–3 AE hits in a 5 s interval).
- The pistons were retracted in a similar manner; σ_1 stress level was reduced to σ_2 and then both were reduced to σ_3 . Finally, all the pistons were retracted to the zero-stress position.
- After removing the injection assembly, the block was cleaned of any excess fluid and the fractured rock was visually inspected for any propagated fractures along the boundaries of the specimen.

2.3 Crack Source Localization

All the recorded AE signals were analyzed to locate AE events, which assisted in mapping the spatio-temporal evolution of fluid induced cracking in granite cubes. The AE events were determined based on the first arrival of the P waves, where the exact arrival of the P wave was determined using the Akaike Information Criterion (AIC) (Maeda 1985). AIC can efficiently separate events (noise and energy motion) in the same time series and has been successfully used to determine the onset time of seismic signals (Kurz et al. 2005; Sleeman and Van Eck 1999). In this study, AE source localization was performed by minimizing the residuals following the procedure described in Li et al. (2019) and Zafar et al. (2022) by comparing the difference in arrival time of AE signals at various sensors. Through this method, AE source locations can be optimized by minimizing the residuals following the equation below:

$$\varepsilon = \sum_{i=1}^N \left| t_i - \frac{\sqrt{(x_o - x_i)^2 + (y_o - y_i)^2 + (z_o - z_i)^2}}{v} \right|, \quad (1)$$

where N is the number of AE sensors, t_i is the arrival time at sensor i , x_o, y_o, z_o are the assumed coordinates of the AE source location, and x_i, y_i, z_i are the coordinates of the position of AE sensors. For v , a constant velocity model of 4000 m/s was used to determine AE events detected by at least six sensors. The AE source location were determined by iteratively searching the values of x_o, y_o , and z_o for which ε will be minimum. The maximum allowed error tolerance was 5 mm (product of ε and v), which was $\sim 3\%$ of the side length of the granite cube (165 mm). Assuming a constant velocity model induced an error in the determined location of AE events. This error was quantified by dropping a steel ball from a controlled height at a known location and assuming a constant velocity model of 4000 m/s. The error in the determined seismic source location after multiple ball drops was ~ 1.4 – 3.6 mm depending on the plane of the specimen, which was below the error tolerance selected for this study (5 mm) (Butt et al. 2023).

2.4 Crack Source Mechanisms

The identification of fracture mechanisms in an HF operation can inform the hydraulic conductivity of the generated fracture and ultimately the efficiency of the stimulation operation. A MT can be used to determine the source mechanisms of seismic events that result from fracturing. A MT is a representation of the source of a seismic event, whereby it describes the equivalent body forces acting at a seismic point source (Burridge and Knopoff 1964). In this study, MT was determined using the Simplified Green's function for Moment tensor Analysis (SiGMA) method, as described in Ohno and Ohtsu (2010), Hampton et al. (2018), Li et al. (2023), and Niu et al. (2023). SiGMA selected only the initial portion of the detected AE signals, from a minimum of six sensors for arrival time, amplitude, and polarity to determine the six independent MT components. A MT contains the properties of a fracture and can be decomposed into double couple (DC), isotropic (ISO), and compensated linear-vector dipole (CLVD) components, where the pure DC component represents shear faulting, and the pure ISO component can be associated with explosive or implosive seismic sources (Knopoff and Randall 1970). A combination of ISO and CLVD components can be representative of the opening or closing of fractures. In this study, the decomposition of MT was performed using the shear-tensile model suggested by Vavryčuk (2001, 2015), which considers the presence of significant non-DC components. Their model does not restrict the slip vector to lying within the fracture

plane and can allow for opening or closing of the fractures/faults. This feature can be particularly important for microseismicity detection during HF, which was found to contain a combination of DC and non-DC components (Baig and Urbancic 2010). The relative proportions of the DC, ISO, and CLVD components can be determined using the following equations:

$$ISO = \frac{1}{2M} (M_1 + M_2 + M_3) \tag{2}$$

$$CLVD = \frac{1}{2M} (M_1 + M_3 - 2M_2) \tag{3}$$

$$DC = \frac{1}{2M} (M_1 - M_3 - |M_1 + M_3 - 2M_2|), \tag{4}$$

where, $M = \frac{1}{2} (|M_1 + M_2 + M_3| + |M_1 - M_3|)$.

$M_1, M_2,$ and M_3 are the eigenvalues of the MT with $M_1 \geq M_2 \geq M_3$ and the sum of |ISO|, |CLVD|, and DC is equal to 1. The ISO and CLVD component can vary from -1 to 1 , whereas DC component can be between 0 and 1 .

Various methods have been employed in the past for laboratory and field HF studies for characterization of individual fracture source mechanisms, which include polarity (Zang et al. 1998), shear-ratio (Ohtsu 1995), DC and non-DC proportions (Vavryčuk 2001), and ISO and CLVD proportions (Davidsen et al. 2021). The Polarity method utilized the sign of first-pulse amplitude, where the polarity value (POL) is calculated as per the following equation (Zang et al. 1998):

$$POL = \frac{1}{n} \sum_1^n \text{sign}(A_i), \tag{5}$$

where A_i is the amplitude of the first motion and n is the number of waveforms detected for each event. If the POL is $-0.25 \leq POL \leq 0.25$, the AE event is classified as shear. For $-1 \leq POL < -0.25$ and $0.25 \leq POL < 1$, the AE event is characterized as tensile and compression, respectively. Using the eigenvalues of the MT determined through the SIGMA method, Ohtsu (1995) classified the crack type based on the shear component (X). The cracks were classified as shear if $X > 60\%$, tensile cracks for $X < 40\%$ and mixed-mode cracks with $40\% < X < 60\%$. The DC–NDC approach is another method where proportion of DC component and the signs of ISO and CLVD are used for the classification of cracks. In this method, AE events with $DC > 50$ are classified as shear, whereby events with $DC \leq 50$ are classified as tensile or compression, depending on the sign of ISO and CLVD component (tensile for positive ISO and CLVD and compression for negative ISO and CLVD). Davidsen et al. (2021) proposed another source mechanism classification method

based on ISO–CLVD proportions. This approach characterizes the fracture as tensile if the ISO component is $\geq 15\%$ and $CLVD \geq -15\%$. The fracture is considered compression if $ISO \leq -15\%$ and $CLVD \leq 15\%$; otherwise, the fracture is considered shear. All these methods divide the seismic sources into shear, tensile, and compression or collapse fractures with the exception of shear ratio, which categorizes them as shear, tensile, and mixed-mode fractures. Readers are referred to the above literature for the details of each classification procedure.

In the current study, the classification of fracture source mechanisms is also performed using the tensile angle (α) which is the angle between normal and slip vector. This parameter can assist in the interpretation of the physical processes especially for the case where a combination of DC, ISO, and CLVD components is encountered in a seismic source (Vavryčuk 2011). The angle α was calculated as per Vavryčuk (2001)

$$\alpha = \sin^{-1} \left(\frac{M_1 + M_3 - 2M_2}{M_1 - M_3} \right), \tag{6}$$

where $M_1, M_2,$ and M_3 are the eigenvalues of the determined MT. This angle can highlight the tensility of the seismic source and is 0° for the pure shear seismic source and $+90^\circ$ and -90° for the pure tensile and compression/compaction sources. However, the correlation between angle α and the non-DC (ISO + CLVD) component is known to be non-proportional, and even a slight rise in angle α can result in a considerable increase in the non-DC component. As per Šílený et al. (2014), the non-DC component surges to approximately 15% and 75% at an angle α of about 3° and 30° , respectively. For the current study, the crack was considered shear if $|\alpha| < 2.5^\circ$, tensile if $\alpha > 2.5^\circ$, and compression for the case $\alpha < -2.5^\circ$.

The rise angle (RA) and the average frequency (AF) method is another technique that can be used to characterize a fracture as a tensile or shear fracture. This RA value, which depends on the time taken to reach the maximum amplitude, can be used to distinguish between the fracture mechanisms. For a tensile fracture, the P-wave magnitude will be larger than that of the S-wave and the rise time will be smaller. The rise time will be much larger for the case of shear fractures with larger S-wave amplitudes. However, the AE sensors used in the current study were dominantly P-wave sensors, which may produce a bias in the favor of P waves. Also, the S-wave arrivals may be impacted by reflections produced from the boundaries of the small-scale laboratory specimens. In addition, a fixed criterion or line between RA/AF has yet to be accepted among researchers to define the proportion of tensile and shear cracks. Due to these limitations, the RA/AF method was not incorporated in this study.

2.5 Dimensionless Toughness Parameter (κ)

According to Detournay (2004), the value of the dimensionless toughness parameter (κ) can ascertain if the propagation occurs in the VPR or TPR in the laboratory. This value is obtained using the basic HF propagation model, involving a planar crack, where the fracture propagates quasi-statically by the injection of a Newtonian fluid at a constant injection rate in opening mode being perpendicular to the minimum principal stress in an elastic medium (Detournay 2016). This dimensionless parameter can be calculated as follows:

$$\kappa = K' \left(\frac{t^2}{\mu'^5 Q_o^3 E'^{13}} \right)^{\frac{1}{18}}, \quad (7)$$

where $K' = \left(\frac{32}{\pi} \right)^{\frac{1}{2}} K_{IC}$, (K_{IC} = Mode-I fracture toughness of the rock); $E' = \left(\frac{E}{1-\nu^2} \right)$, (E = Young's modulus; ν = Poisson's ratio); $\mu' = 12\mu$ (μ = fracturing fluid viscosity); t = fracture propagation time; Q_o = rate of fluid injection. For $\kappa \leq 1$, the VPR dominates; and for $\kappa \geq 3.5$, the TPR dominates (Savitki and Detournay 2002). The grain size of the host rock influences the fracture toughness and dilatancy properties and may have a more significant effect for laboratory fracturing compared to the field; however, micro-structural scaling was found to be impractical, as reported by De Pater et al. (1994a, b) and was not considered in the present study.

The required inputs for determination of κ are the mechanical properties of the rock, the rate and viscosity of the fluid, and the fracture propagation time. The material properties of the Barre granite (Table 1) were used to determine the dominant propagation regime. Fluids with different viscosities [water (1 cP) and SAE 85w-140 (Super Tech Co.) gear oil (1450 cP)] were used for the HF experiments, where both fluids were injected at a constant injection rate of 1 ml/min. The viscosity of gear oil was determined using a discovery hybrid rheometer (DHR)-3 in the laboratory at 20 °C and was found to be 1450 ± 5 for a wide range of shear rates (1–100 1/s), indicating a Newtonian behavior. Also, the viscosity of fluids can be pressure-dependent (especially gear oil), where viscosity generally increases with the increase in pressure (Schmelzer et al. 2005). However, the change in viscosities is expected to be small for the pressure ranges (15–25 MPa) of the fluids in our experiments (Bair 2016; Bett and Cappi 1965; Nakamura 2016).

The fracture propagation time is an input parameter that determines the dominant propagation regime, which is the time from the fracture initiation to the end of fracture propagation (fracture reaching the boundaries of the specimen in laboratory experiments). It is imperative to determine this period accurately from the fracture initiation to fracture arrival at the boundaries of the laboratory

specimen as it will determine the value of κ and the corresponding state of HF. Most of the past laboratory studies determined this experiment time from the borehole pressure curve alone. However, minor changes in pressure due to the fluid flow in the generated fracture may make it difficult to estimate. In those cases, other supplemental techniques, such as AE monitoring, can be useful in finding this time period. In this study, the fracture propagation time was determined using both the pressurization rate and the detected AE data (see Sect. 3.1 for more details).

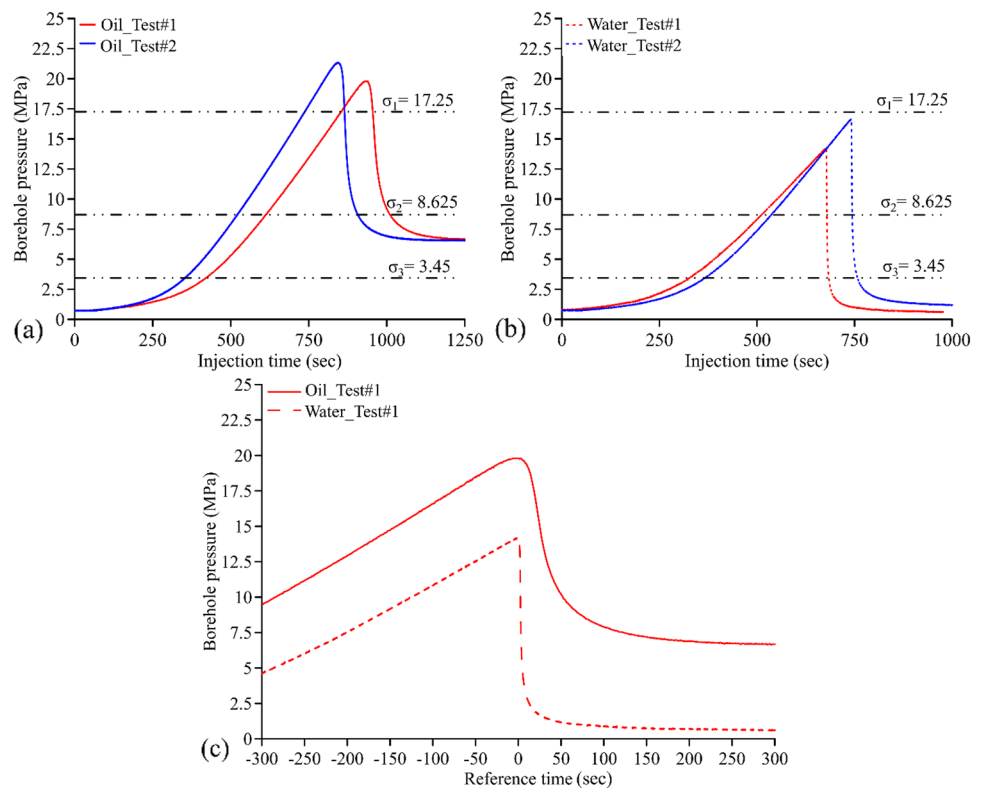
3 Experimental Results

3.1 Well-Bore Pressure Decay Analysis

The borehole pressure evolution for high- and low-viscosity injection fluid experiments is presented in Fig. 3a and b. Two tests each were conducted for the oil and water to confirm the repeatability of the results. Since the time to reach BP was dissimilar for different fluids, a reference time was calculated by subtracting the BP time (time at breakdown pressure) from the experimental time. Negative values for the reference time indicated the pre-breakdown stage of the experiment, while positive values indicated the post-breakdown stage. Figure 3c presents the pressure evolution against the reference time for one oil and one water experiments, and we therefore present our detailed results and analysis for those two experiments.

The system's compliance can have a significant impact on HF and its propagation (Ito et al. 2010). Before evaluating the distinct fracture propagation behavior and characteristics, it is important to determine the system compressibility values for different injection fluids. Our injection system consisted of stiff stainless-steel tubing and connectors and was identical for both the oil and water experiments. Therefore, system compliance mainly depended on fluid compressibility, which was determined from the inverse of the borehole pressure and the injected fluid volume (Ito et al. 2006). While the viscosities of gear oil and water were different, the pressurization rates were found to be almost identical for both the oil (2.2 MPa/sec) and water (2 MPa/sec) experiments. Both fluids were injected at the same constant rate (1 ml/min), which also resulted in similar values of system compressibility (0.46 and 0.51 ml/MPa for the oil and water, respectively). These values are lower than those calculated for a stiff system in the field by Ito et al. (2006) and therefore can be representative of a system with minimum system compliance. Figure 3 presents the evolution of the borehole pressure, pressurization rate $\left(\frac{dP}{dt} = \frac{P_2 - P_1}{t_2 - t_1} \right)$, and

Fig. 3 Borehole pressure evolution with actual experimental time for **a** oil and **b** water experiments. **c** Borehole pressure evolution against reference time for a pair of oil and water experiments



Q_{in} , which represents the fluid flowing inside the generated fracture. Q_{in} was calculated using system compressibility C , $\frac{dP}{dt}$, constant flow rate (Q_o) following Lecampion et al. (2017):

$$Q_{in} = Q_o - C \frac{dP}{dt} \tag{8}$$

Figure 4 shows that the BP was lower (28%) for the water experiment. However, the difference between oil and water was much more drastic when comparing the $\frac{dP}{dt}$ and Q_{in} . The drop in $\frac{dP}{dt}$ and the increase of Q_{in} were nearly an order of magnitude greater for the water experiment than for the oil experiment.

The fracture propagation time (time from initiation to fracture reaching boundaries), which is an important parameter in determining the dominant propagation regime, was determined using $\frac{dP}{dt}$ and the detected AE hits. Figure 5 presents the AE rates against the borehole pressure evolution and $\frac{dP}{dt}$ for the oil and water experiments. Fracture initiation (FI) was identified following the increase in the AE rate and was detected earlier by the AE system, where no significant change in the borehole pressure with experimental time or $\frac{dP}{dt}$ could be observed. The fracture reaching the boundaries of the specimen (FRB) was deduced from the lowest point of $\frac{dP}{dt}$ and the cumulative AE hits reaching almost constant values. These fracture propagation times were quite different from those

determined through the pressure curve analysis alone (departure from linearity to a constant value after BP). Table 2 lists the fracture propagation times (from FI to FRB) along with other hydro-mechanical findings for the oil and water experiments.

3.2 Determination of Dominant Propagation Regime

The values of the dimensionless toughness parameter (κ), Eq. (4), with varying experimental conditions (different fluids and fracture propagation times) are presented in Fig. 6. Based on the fracture propagation times (Table 2) determined after the experiments, the κ values were determined for experiments performed with high- and low-viscosity injection fluids. The determined κ values and the corresponding propagation regimes for dissimilar experimental conditions are presented in Table 2, where a value of 0.85 represents a viscosity-dominated propagation regime and a value of 4.8 indicates that the fracture was propagating in the toughness-dominated regime. While the material properties (E , K_{IC} , and ν) used in the determination of dominant propagation regime were taken from the literature, $\pm 10\%$ variation in these properties still resulted in the same propagation regimes. (0.76–0.93 for oil and 4.3–5.3 for water for $\pm 10\%$ variation in E , K_{IC} , and ν). It also can be observed from Fig. 6 that slight errors in the determination of fracture

Fig. 4 Evolution of borehole pressure, pressurization rate (dP/dt), and fluid flow into the fracture (Q_{in}) for **a** Oil_Test#1 and **b** Water_Test#1. Note the difference in scale of dP/dt and Q_{in} between oil and water experiments

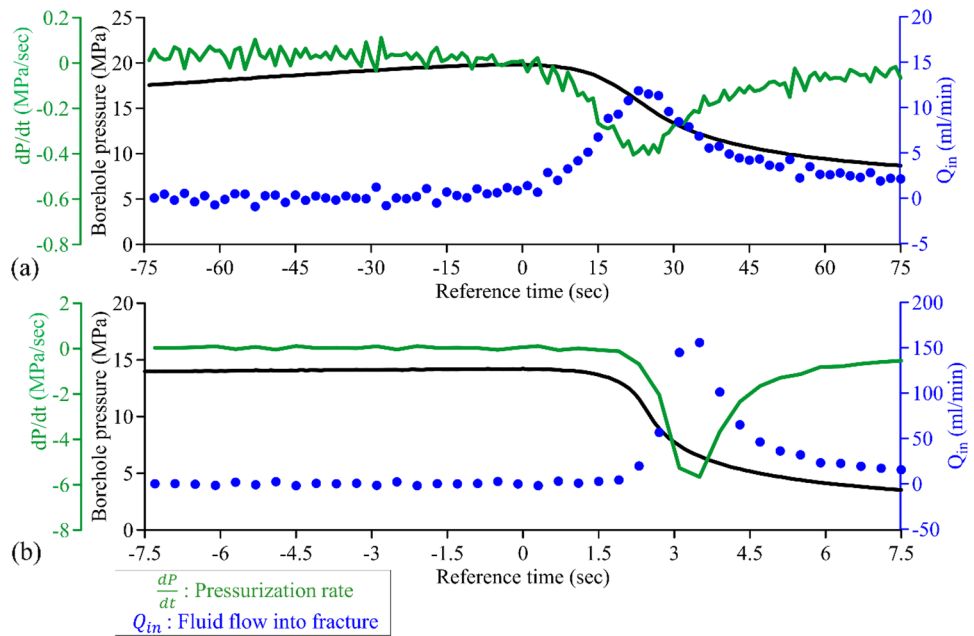
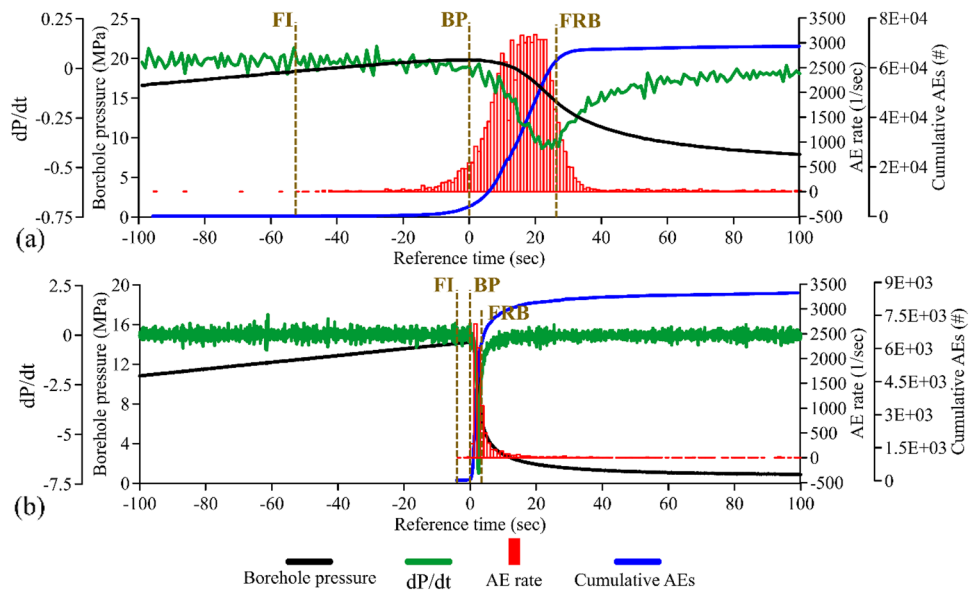


Fig. 5 AE rate and cumulative AE hits along with the borehole pressure evolution and pressurization rate (dP/dt) against reference time for **a** Oil_Test#1 and **b** Water_Test#1; FI (fracture initiation) represents the point where the AE rate started to increase, BP (breakdown pressure) was the highest recorded borehole pressure for a particular experiment, and FRB (fracture reaching boundaries of the specimen) was determined using the pressurization rate (dP/dt) and the cumulative AE hits



propagation times did not impact the resulting dominant fracture propagation regimes.

3.3 Spatiotemporal Evolution of AE Events

The spatio-temporal evolution of the AE events during the HF experiments is presented in Figs. 7 and 8 for oil and water, respectively. The moment magnitude (M) was determined using the seismic moment (M_o) which was obtained after calibration of the AE sensors following Wu et al. (2021). The following relationship was used to determine moment magnitude M_w (Hanks and Kanamori 1979):

$$M_w = \frac{2}{3} \log_{10} M_o - 6. \tag{9}$$

After fracture initiation, accompanied with the increase in detected microseismicity, HF propagated stably and steadily until BP, which was followed by unstable fracture propagation and a rapid decrease in the borehole pressure. In laboratory experiments, with finite specimen dimensions, this unstable fracture propagation terminated when the fracture reached the boundaries of the specimen. However, even after the fracture reached the boundaries of the specimen, some residual fracturing continued until the borehole pressure reached a constant

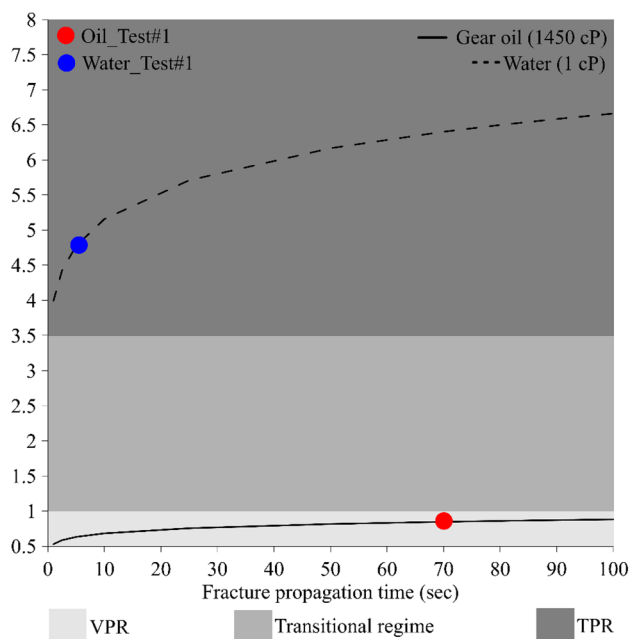


Fig. 6 The evolution of dimensionless toughness parameter, κ , with the fracture propagation time determined for high- and low-viscosity fluids. The points highlighted in the graph indicates the determined state of the HF operation for experiments conducted for this study using oil and water; κ value of 0.85 corresponded to a viscosity-dominated propagation regime, whereas κ value of 4.8 resulted in the toughness-dominated propagation regime

value. For all the experiments, the complete propagation of HF occurred in three distinct phases: (I) initiation to breakdown, (II) breakdown to fracture reaching the boundaries of the specimen, and (III) post-fracturing until the end of the experiment. For both the oil and water experiments, phase-I consisted of relatively small-magnitude AE events surrounding the

borehole (Figs. 7 and 8). High-magnitude AE events occurred mostly in phase-II along with a sudden drop in borehole pressure. The number of AE events detected for water experiments (352) was lower compared to the oil experiment (1495) in all the phases of the experiments. The AE events were found to be relatively more homogeneously distributed for the oil experiment, while more of the detected AE water experiment events were concentrated on one side.

3.4 Determination of Gutenberg–Richter b -value

The Gutenberg–Richter (GR) b -value for the frequency–magnitude distribution of the AE events determines the ratio between the large and small seismic events and is a fundamental observation in seismology and seismic risk analysis. The GR distribution relates the number of seismic events (N) equal to or greater than a given magnitude to the magnitude of the event (M) (Gutenberg and Richter 1944)

$$\log(N) = a - bM, \tag{10}$$

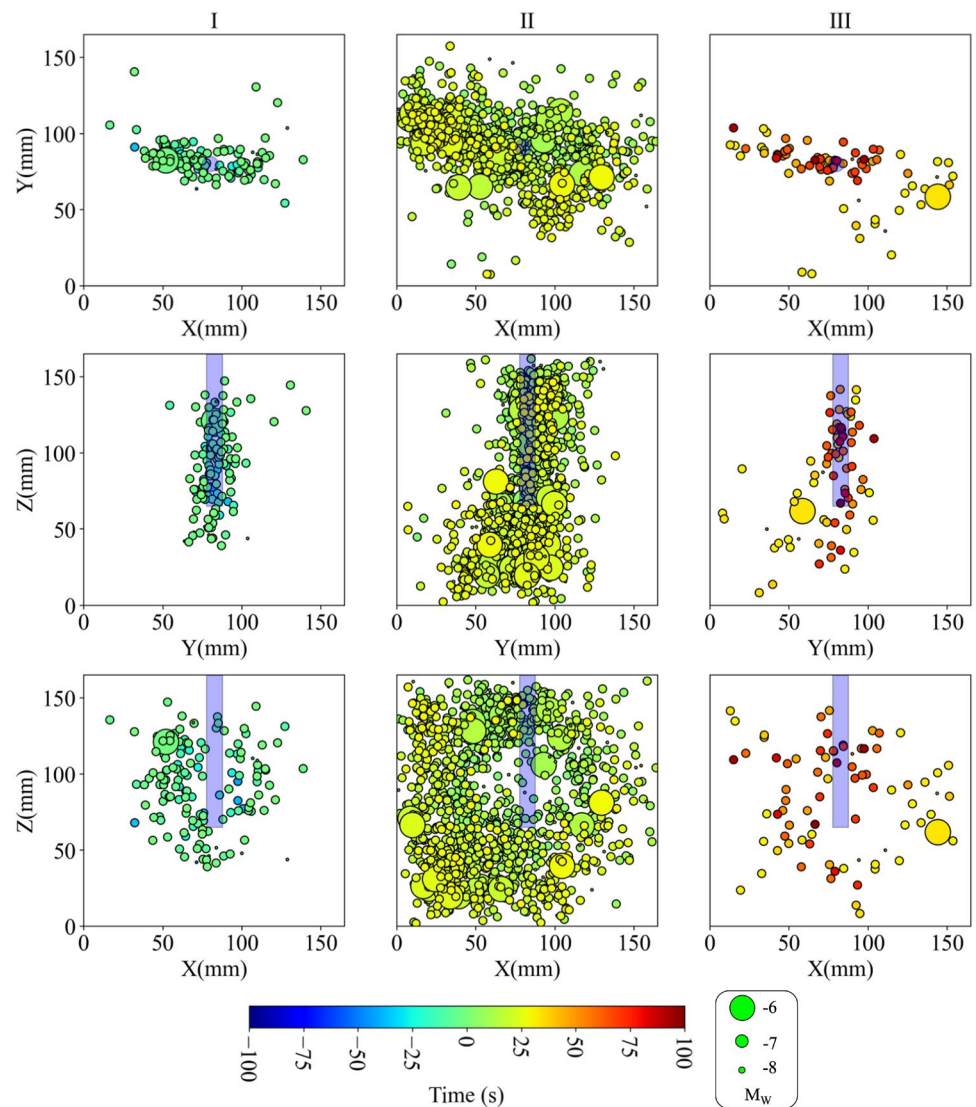
where a and b are constants, which depends on the seismicity rate and properties of the material, respectively (Olsson 1999) and M is the moment magnitude (M_w) determined using Eq. 9. A higher b value corresponds to a higher frequency of small magnitude events, whereas a lower b value points towards the relative abundance of higher magnitude events. In this study, b values were calculated using the maximum-likelihood method described by Aki (1965), Utsu (1965), and Woessner and Wiemer (2005)

$$b = \frac{\log_{10}(e)}{\left[\langle M \rangle - \left(M_c - \frac{\Delta M_{bin}}{2} \right) \right]}, \tag{11}$$

Table 2 Experimental parameters and results for oil and water experiments

Properties	Oil_Test#1	Water_Test#1
Modulus of elasticity (GPa)	60	
Mode-I fracture toughness (MPa. (m) ^{1/2})	1.14	
Injection fluid	SAE 85w-140 gear oil	Water
Fluid viscosity (cP @ 20 °C and 1 atm)	1450	1
Flow rate (Q_o) (ml/min)	1	
Pressurization rate (MPa/min)	2.2	2.0
Compressibility (ml/MPa)	0.46	0.51
Propagation time through pressurization rate and AE data (sec)	70	5.5
κ	0.85	4.8
Propagation regimes	Viscosity-dominated regime	Toughness-dominated regime

Fig. 7 Spatiotemporal evolution of the AE events at different stages of the HF for Oil_Test#1; Phase (I) initiation to breakdown, (II) breakdown to fracture reaching boundaries of the specimen, and (III) the post-fracturing phase. The color of the circles represents the temporal evolution, whereas size of the circles represents the moment magnitude (M_w) of the AE events



where M_c , $\langle M \rangle$, and ΔM_{bin} are the magnitude of the completeness, mean magnitude, and the binning width of the seismic data, respectively. M_c is defined as the lowest magnitude at which 100% of the seismic events can be detected in space and time volume (Rydelek and Sacks 1989; Wiemer and Wyss 2000). In the current study, M_c was determined using the Woessner and Wiemer (2005) method which identifies the point of maximum curvature by computing the maximum value of the first derivative of the frequency–magnitude curve. This maximum curvature point, taken as M_c , is a fast estimate which has been reliably and successfully applied to natural earthquakes sequences (Gulia and Wiemer 2019), using the slope of the logarithm of the cumulative number of the detected seismic events (i.e., $\{\log(\Sigma N)\}$). The ΔM_{bin} was set to 0.05 and the minimum number of AE events required for the determination

of b value was set to 50. The b values were determined for the three phases that were identified in Sect. 3.3, for both the oil and water experiments (Fig. 9). For both experiments, b value ≥ 2 were encountered, where phase-I was characterized by having larger values. The b values tended to decrease in phase-II, followed by a slight increase in phase-III.

3.5 Identification of Fracture Source Mechanisms

Figure 10a–c presents the histograms highlighting the number of AE events with varying proportions of the ISO, CLVD, and DC components obtained through the decomposition of MT as per Eqs. 2–4. Despite observing similarities in different components for both the oil and water experiments, we noticed distinct variations. The number of seismic events with larger DC proportions was greater for

Fig. 8 Spatiotemporal evolution of the AE events at different stages of the HF for Water_Test#1; Phase (I) initiation to breakdown, (II) breakdown to fracture reaching boundaries of the specimen, and (III) the post-fracturing phase. The color of the circles represents the temporal evolution, whereas size of the circles represents the moment magnitude (M_w) of the AE events

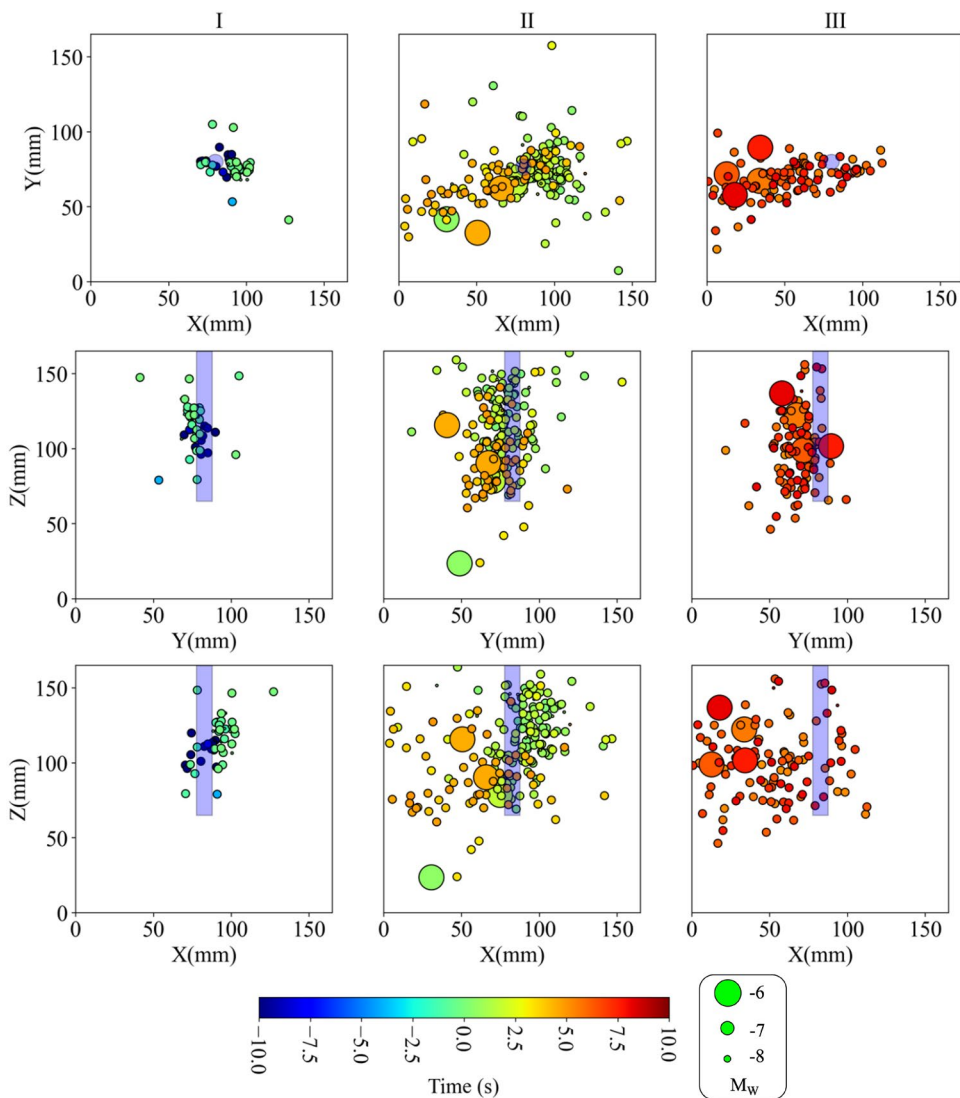


Fig. 9 b value calculation for different phases for the **a–c** Oil_Test#1 and **d–f** Water_Test#1 experiments. N is the number of seismic events equal to or greater than a given magnitude (M). M is the moment magnitude and ΔM_{bin} was selected as 0.05. The b value was determined for the linear portion of the $\log(\Sigma N)$ (logarithm of the cumulative N) and the M plot

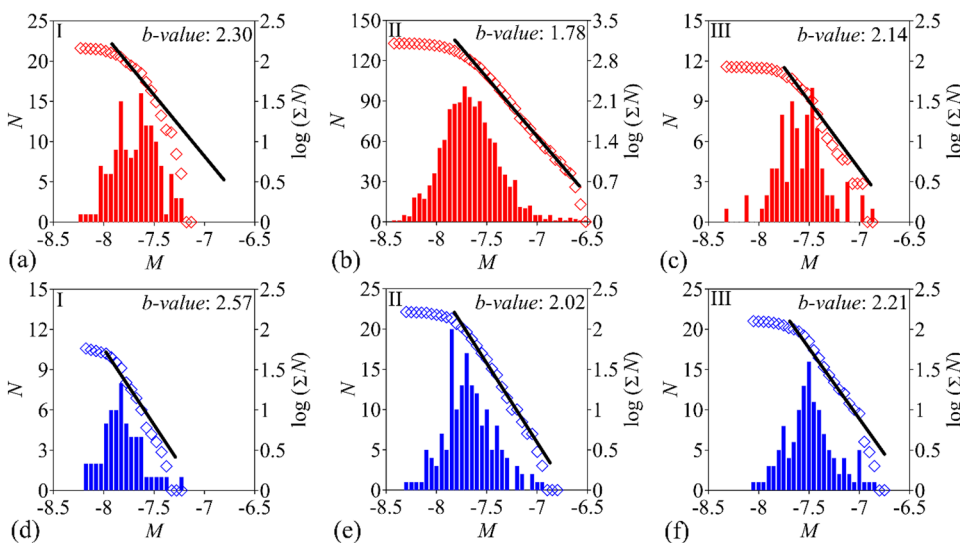
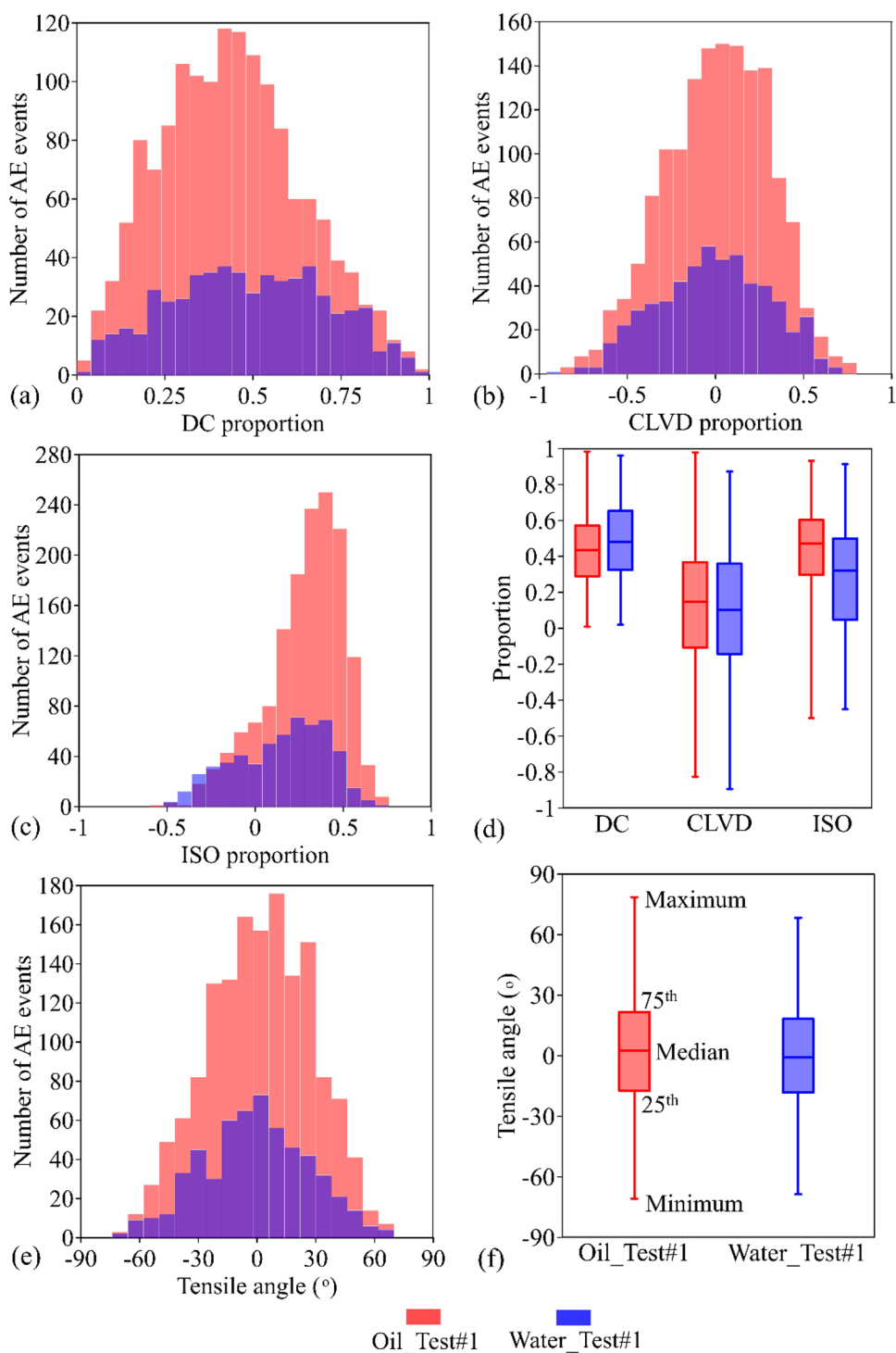


Fig. 10 Histograms of AE events detected for Oil_Test#1 and Water_Test#1 with different proportions of **a** ISO, **b** CLVD, **c** DC components, and **e** tensile angle determined through MT decomposition. The box plots presenting the median, range, and quartiles of the data are also presented for **d** DC/CLVD/ISO components and the **f** tensile angle



the water experiment (Fig. 10a). A relatively greater number of seismic events with negative ISO components were also detected for the water experiment (Fig. 10c); and the CLVD component was comparable for both the oil and water experiments (Fig. 10b). These differences also can be seen from the box plots representing the minimum, maximum, median, and quartiles for both experiments (Fig. 10d). The α angle

was determined for the AE events, and their distribution is presented in Fig. 10e and f for both experiments. Figure 10f shows that the α angle varied between $\pm 3^\circ$ and $\pm 30^\circ$ for the majority of AE events. The percentage of AE events with $\alpha < \pm 3^\circ$ and $\alpha > \pm 30^\circ$ for the oil HF experiment was 8% and 27%, respectively. For the water experiment, these percentages were similar at 12% and 30%. Another method

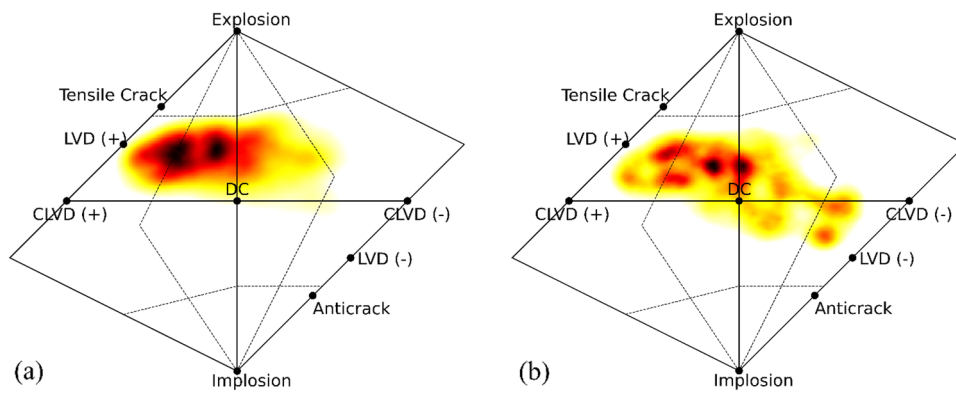


Fig. 11 Hudson plots for the MT solutions for the **a** Oil_Test#1 and **b** Water_Test#1 HF experiments. The explosion and implosion represent isotropic or hydrostatic sources with zero CLVD and DC component. DC represents pure shear faulting on a non-planar fault with

zero volumetric (ISO and CLVD) component. The tensile crack and anticrack are tensile and compressive cracks with zero DC. The similar positive or negative signs of ISO and CLVD characterize the crack as tensile crack or anticrack, respectively

for qualitatively classifying the faulting style is source-type plotting following Hudson et al. (1989). In this study, the Hudson plots were generated through the MATLAB package provided in Kwiatek et al. (2016). This package produced skewed diamonds plots using the proportions of ISO and CLVD components to ascertain the faulting style during both the oil and water experiments (Figs. 11a and b). It can be seen in Fig. 11a that a majority of the seismic events had positive ISO and CLVD components for the oil experiment. In contrast, the water experiment displayed a combination of positive and negative ISO and CLVD components (Fig. 11b). Following the classification suggested by Frohlich (2001) and Martínez-Garzón et al. (2017), these distinct types of behaviors observed for oil and water can be classified as normal and oblique faulting, respectively.

or proportions of source mechanisms obtained through the different techniques were found to be quite dissimilar. For example, for oil, a majority (82%–88%) of the events were classified as tensile using the Polarity method. However, with shear ratio, this dominance was reduced to almost half (43%–45%) for the same HF experiment. For water, the difference in the percentages of tensile and shear fractures was significantly small (4%–5%) if the classification was based on DC and non-DC proportion (Vavryčuk 2001) relative to other techniques. Nevertheless, despite these variations, the general patterns were comparable. Nearly all the techniques showed that the tensile fractures were predominant for both the oil and water HF experiments. However, the proportion of tensile fractures decreased, and the proportion of shear and compression fractures increased for the HF experiments with low-viscosity water injections.

Figure 12 and Table 3 present the percentages of fracture source mechanisms classified individually through various procedures (described in Sect. 3.4) for the oil and water experiments. To confirm the repeatability of results, we conducted two separate experiments for oil and water, the findings of which are shown in Table 3. The percentages

Figures 13 and 14 present the spatio-temporal evolution of fracture mechanisms during the HF experiments conducted with oil and water, respectively. All the AE events were classified as tensile, compression, or shear based on the ISO–CLVD proportions presented in Davidsen et al.

Fig. 12 The distribution of fracture source mechanisms as shear, tensile, and compression determined using different classification criteria for the **a** Oil_Test#1 and **b** Water_Test#1 HF experiments. The mean values are also presented for different fracture mechanisms

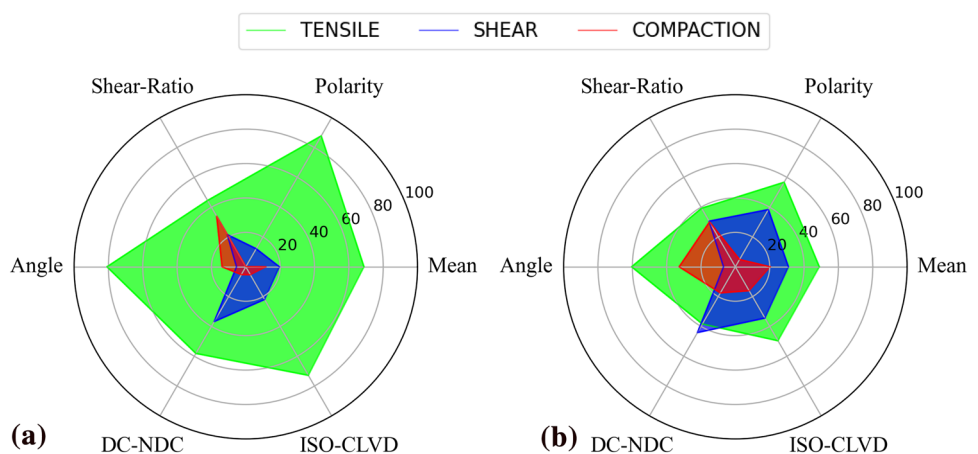
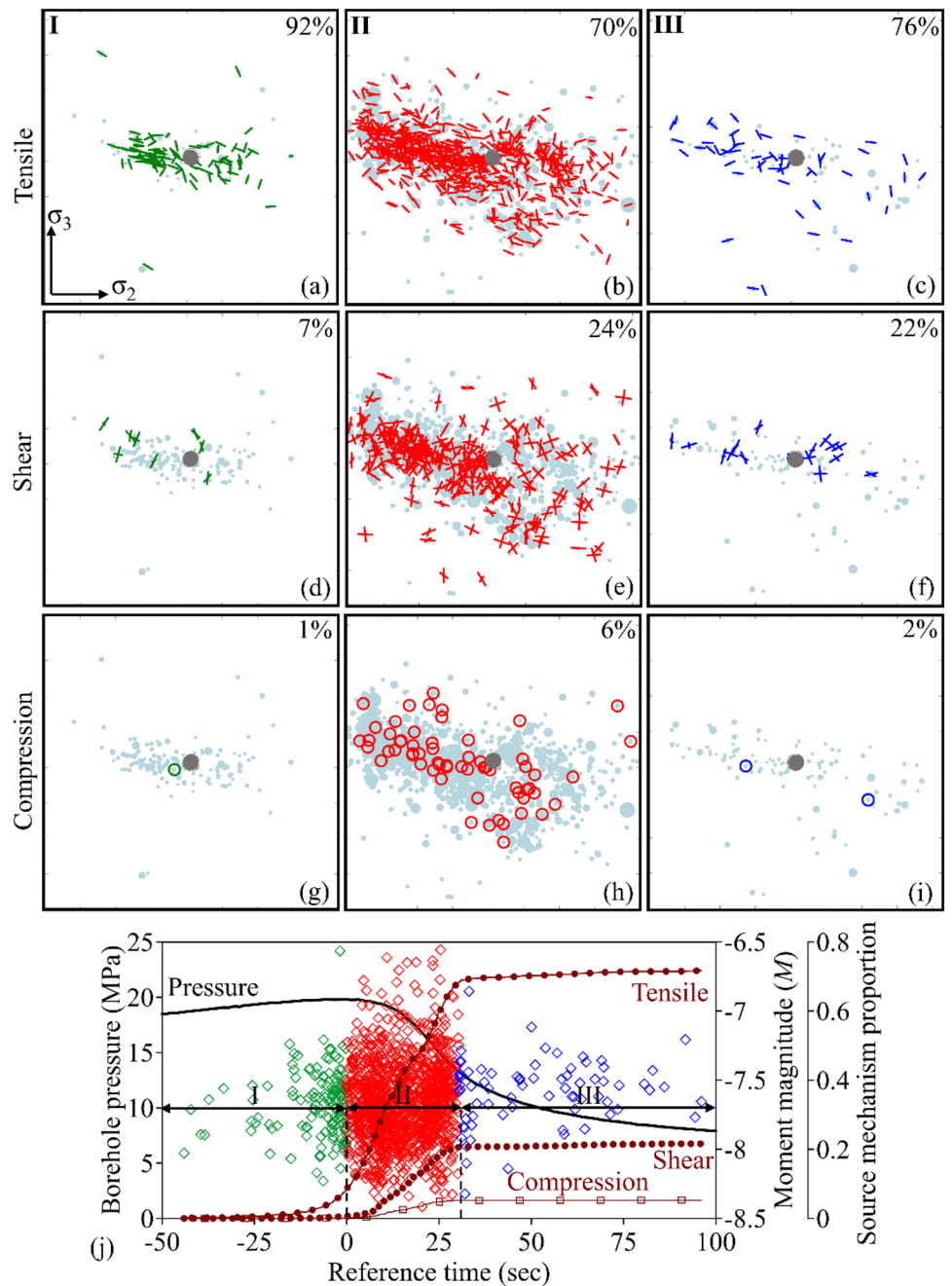


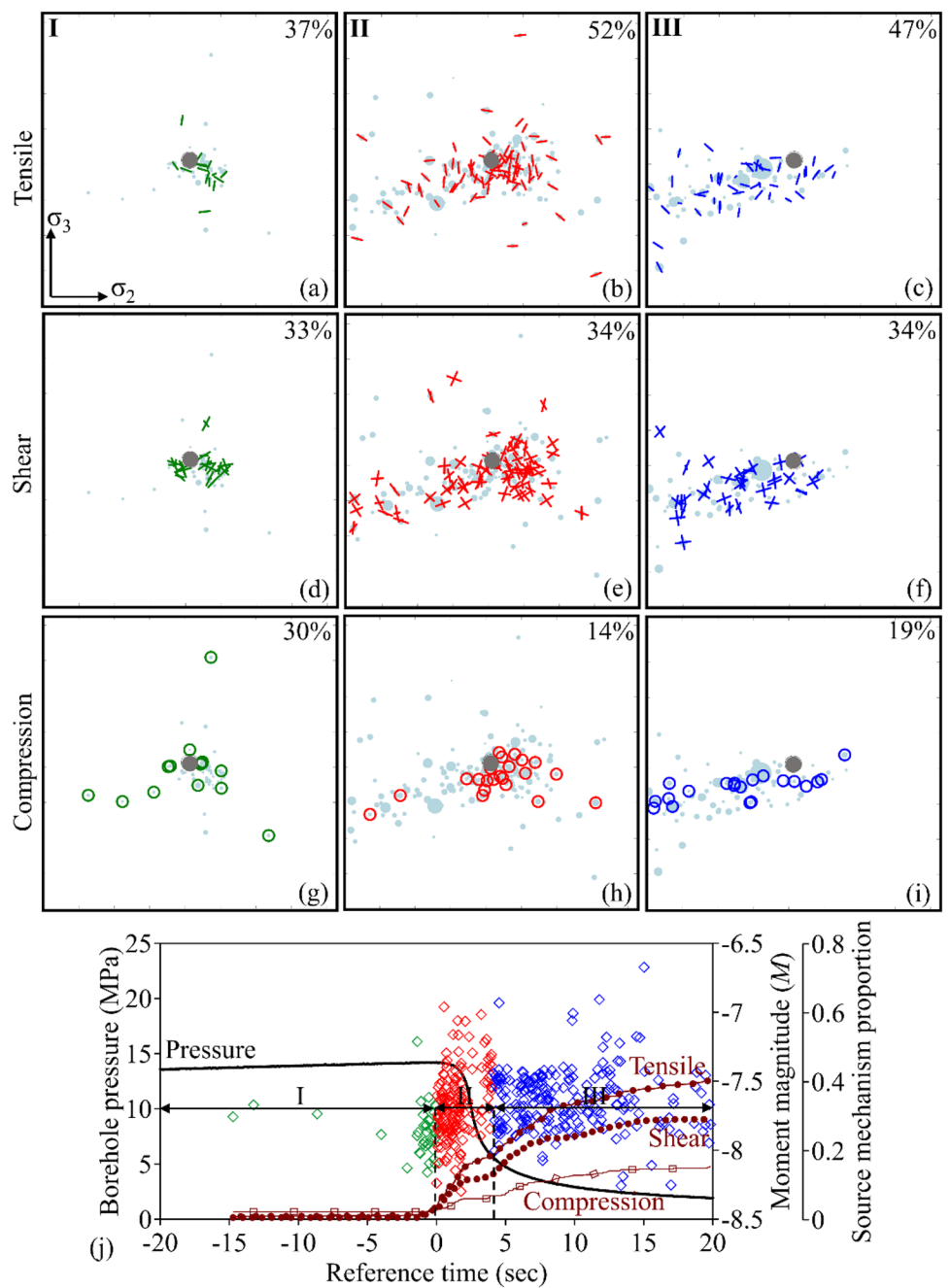
Fig. 13 The evolution of crack source mechanisms during the three phases of Oil_Test#1 experiment, determined based on the ISO–CLVD method; tensile (a–c), shear (d–f), and compression (g–i) mode, along with the percentages, in the top, middle, and bottom rows, respectively. The color of the symbols corresponds to the particular fracturing phase. In j, \diamond symbol represent the evolution of moment magnitude in different phases of the experiment. The dark red-color lines indicate the evolution of source mechanism proportion (tensile, shear, and compression) (Colour figure online)



(2021). Tensile fractures were dominant for both the oil and water experiments in all phases; however, the percentages were different for oil and water. For the oil experiment, the majority of tensile fractures (92%) were observed near the borehole during phase-I of the oil experiment (Fig. 13). The percentage of shear events (7%) was lower with almost negligible compression events (1%). While tensile events continued to remain dominant during phase-II and phase-III of the oil experiments, the percentage of compression and shear

events slightly increased. For the water experiment (Fig. 14), the percentage of tensile events remained the highest; however, the percentage of shear and compression events were found to be higher for all phases of the experiments. The most significant increase was observed during phase-I of the experiments, where the proportion of shear and compression events was 33% and 30% for water compared to only 7% and 1% for oil.

Fig. 14 The evolution of crack source mechanisms during the three phases of Water_Test#1 experiment, determined based on the ISO–CLVD method; tensile (a–c), shear (d–f), and compression (g–i) mode, along with the percentages, in the top, middle, and bottom rows, respectively. The color of the symbols corresponds to the particular fracturing phase. In j, \diamond symbol represent the evolution of moment magnitude in different phases of the experiment. The dark red-color lines indicate the evolution of source mechanism proportion (tensile, shear, and compression) (Colour figure online)



4 Discussion

4.1 Difference in Hydro-mechanical Response and Fracture Profiles Characteristics

Table 4 presents a general summary of the hydro-mechanical and seismicity results for our oil and water experiments.

On average, higher BP and injected volume were observed for the oil experiments, as similarly observed for granitic rocks with high-viscosity fluid (e.g., Ishida et al. 2016). The injected volume until BP was calculated by multiplying the constant injection rate with the time to reach the BP for a particular experiment. It can be deduced from Figs. 3 and 4 that the pressure decay was abrupt for water experiments and the fracture propagation time was almost an order of

Table 3 Summary of focal mechanisms results for oil and water experiments following different classification criteria

Injection fluid		Oil		Water	
Methods	Fracture mechanism (%)	Test#1	Test#2	Test#1	Test#2
Polarity	Shear	12.1	17.3	38.4	30.9
	Tensile	87.8	81.9	56.7	65.5
	Compaction	0.1	0.8	4.9	3.5
Shear-ratio	Shear	21.6	21.3	30.6	25.3
	Tensile	44.5	43.0	39.3	34.9
	Mixed	33.9	35.7	30.1	39.8
DC-NDC	Shear	36.7	32.6	44.1	41.0
	Tensile	58.1	62.2	38.4	46.1
	Compaction	5.2	6.2	17.5	12.9
ISO-CLVD	Shear	21.9	23.0	34.4	31.4
	Tensile	72.8	71.5	49.6	55.3
	Compaction	5.3	5.5	16.0	13.3
Tensile angle (°)	Shear	5.4	5.6	6.9	3.3
	Tensile	80.8	81.1	60.4	61.5
	Compaction	13.8	13.3	32.7	34.2

magnitude smaller than for oil experiments. This sudden pressure drop resulted in a temporary increased injection rate, which represents the fluid flowing inside the generated fracture (Q_{in}). Figure 4 indicates that the Q_{in} for the water experiment increased almost instantly to a much higher value (155 ml/min) compared to the oil experiments (12 ml/min). This high fluid entering rate in the fracture, for the water experiments, was attributed to its low viscosity with negligible viscous resistance compared to oil. Our results were in line with past results by Lecampion et al. (2017) for laboratory HF experiments in VPR and TPR conditions using PMMA and cement blocks. In the field, it is also expected that the pressure drop and Q_{in} for TPR experiments, which are conducted with low-viscosity gas, would be much higher relative to the VPR experiments.

In the field, fractures initiate and propagate near the wellbore plug, which is the zone of stress concentration (Hampson et al. 2013), whereas in the laboratory, the stress concentration occurs near the top and bottom edges of the open

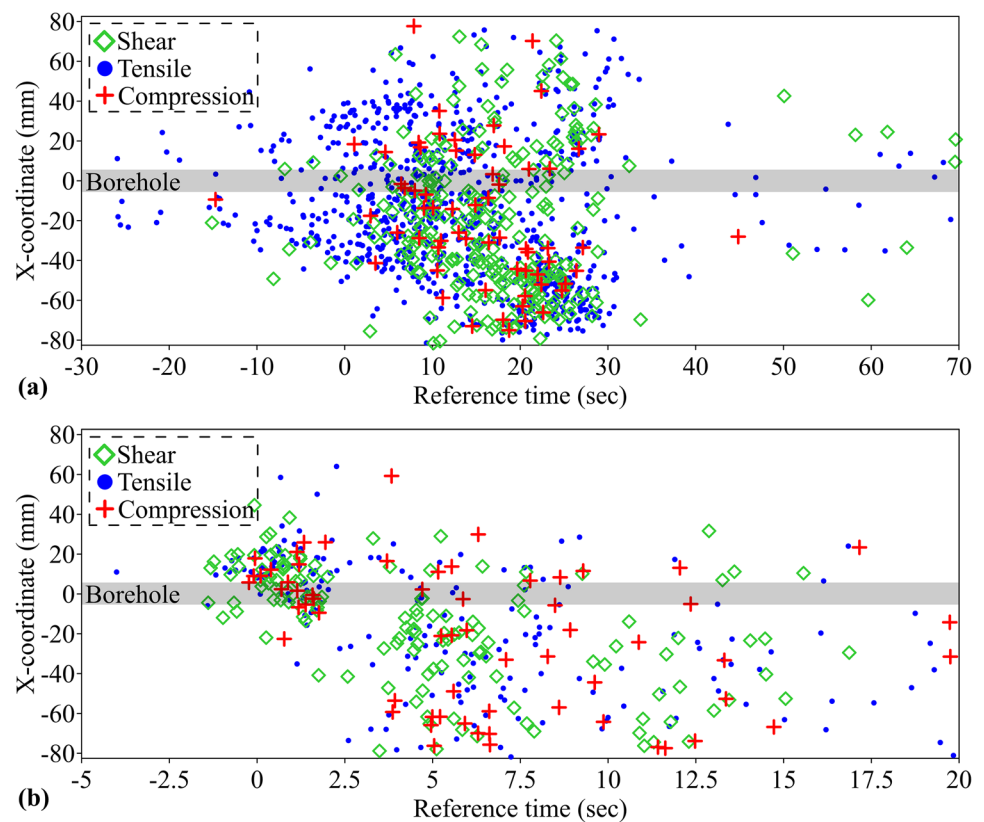
borehole region. For oil experiment (Fig. 7), the AE events in the fracture initiation phase (pre-BP) occurred in almost a circular region perpendicular to σ_3 , surrounding the open injection section. For the water experiments (Fig. 8), the AE events were encountered on one side near the top edge of the injection section, which is known to be a zone of stress concentration. These results indicate that HF propagation for TPR situations, with much lower viscosity fluids, will be affected much more by the areas of stress concentration and local heterogeneity relative to VPR with high-viscosity fluids. With regard to the HF propagation, it can be deduced from the spatio-temporal evolution of the AE events that the fracture propagated almost symmetrically for the oil experiments (Fig. 7), but it propagated in one direction only for the water experiment (Figs. 8). The AE events were found to occur almost in concentric circles moving away from the injection borehole for the oil experiments. In comparison, for the water experiments, most of the AE events occurring during phase-II and -III were in a different direction than

Table 4 Hydro-mechanical and seismicity results for oil and water experiments

Injection fluid	Test number	BP (MPa)	Injected volume till BP (ml)	Number of AE events (#)	Larg-est moment magnitude (M_w) event	<i>b</i> value		
						I	II	III
Oil	1	19.80	15.62	1495.00	− 6.58	2.30	1.78	2.14
	2	21.30	14.05	1130.00	− 6.63	2.40	1.83	2.08
Water	1	14.20	11.31	352.00	− 6.80	2.57	2.02	2.21
	2	16.40	12.29	215.00	− 6.95	−*	2.14	2.40

*The number of AE events (24) were less than 50 for the determination of *b* value

Fig. 15 Temporal evolution of damage mechanisms (shear, tensile, and compression) with distance (X-coordinate) from the borehole for **a** Oil_Test#1 and **b** Water_Test#1 determined based on ISO-CLVD method. The distance is from the center (0) to the boundaries of the specimen in the direction of fracture propagation



the AE events detected during phase-I. This microseismicity detected haphazardly on either side of the injection borehole pointed towards a more heterogeneous propagation of HF for the TPR conditions. Ishida et al. (2021) conducted a small-scale HF field experiment using CO₂ in a railroad tunnel in Japan. The fracture geometry was similar to our observations in the water experiments representing TPR conducted in this study, where fractures propagated more on one side of the injection hole than the other. Huang et al. (2019) numerically analyzed the difference in the fracture profiles for VPR and TPR conditions using discrete-element modeling; and for TPR settings, their resulting fractures were more asymmetrical with one wing being arrested, similar to the results obtained in this study for water experiments (Fig. 8).

4.2 Characteristics of Microseismicity for Different Injection Fluids

Depending on the techniques that are used to classify the source mechanisms into shear, tensile, and compaction, the results varied significantly (Fig. 12). However, regardless of the technique used to identify the fracture mechanisms, the current study revealed that tensile fracturing events were prevalent for both high- and low-viscosity injection fluids in all experiments (Figs. 13 and 14 and Table 3). Nevertheless, the percentage of tensile fracturing events varied between

the two injection fluids and as the HF propagated away from the injection source. Figure 15 presents the evolution of the fracturing mechanisms from the borehole until the boundaries of the specimen in the direction of fracture propagation. The strong tensile dominance for the oil experiment in the pre-BP stage (Figs. 13 and 15a) can be attributed to expansive dilation of the region surrounding the borehole due to highly pressurized fluid and minimal fluid permeation as reported by Schmitt and Zoback (1992) for Westerly granite cylinders and even for Nash Point Shale by Gehne et al. (2019). For the pre-BP stages in the water experiments, the majority of events were also found to be tensile events (Figs. 14 and 15b); however, the percentage of tensile events was lower than for the oil experiments. This outcome can be attributed to the low viscosity of water, which can permeate the region surrounding the pressurized borehole, resulting in limited dilation of the region surrounding the injection location. The high percentage of compression events detected for our water experiments was similarly encountered for a small-scale field HF experiment conducted with CO₂, representing TPR conditions (Ishida et al. 2021). The HF propagated sub-parallel to the σ_2 -direction for both oil and water, deviating slightly from planarity, as can be observed from the spatio-temporal distribution of AE events for the oil and water experiments (Figs. 7 and 8). This deviation may have been caused by the anisotropy of the Barre granite specimens

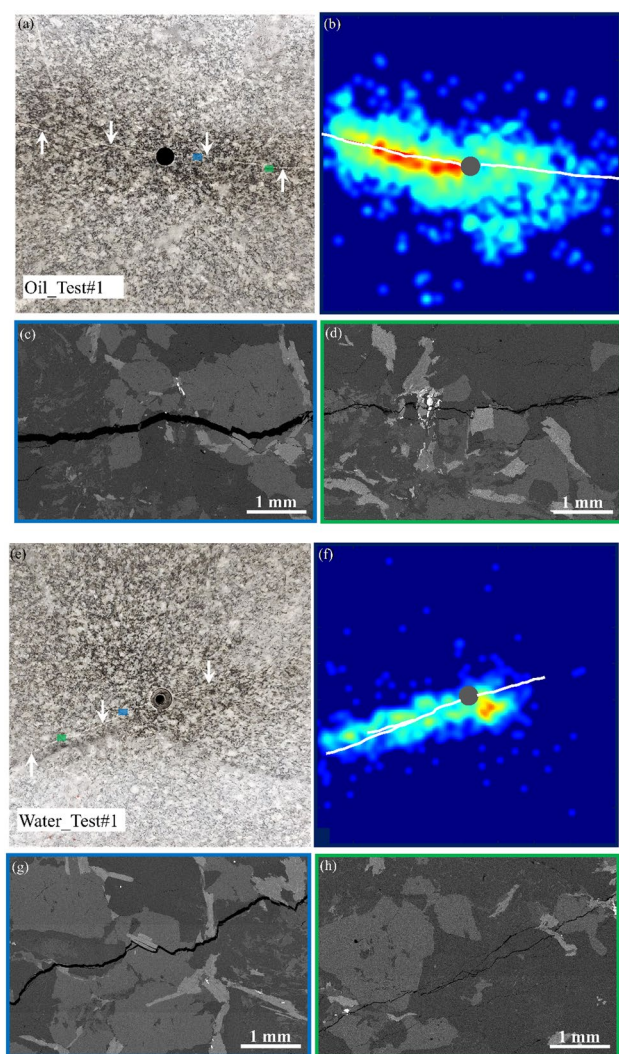


Fig. 16 The actual HF generated related to the determined AE events (density maps) for the **a, b** Oil_Test#1 and **e, f** Water_Test#1 experiments. For the images of the HF, specimens were cut at midpoint perpendicular to the fracture plane. The arrows and white line highlight the location of HF in **a/e** and **b/f**, respectively. Zoomed-in segments of HF closer (blue) (**c** and **g**) and farther (green) (**d** and **h**) from the injection borehole are also presented for both the experiments (Color figure online)

where different planes of weakness (hardway, grain, and rift) may not be exactly in line with the stress directions. As the HF propagated in the granite specimens, the percentage of tensile events varied both for high- and low-viscosity fluids with higher numbers of shear fractures encountered mostly away from the injection borehole region (Fig. 15). In addition, as the HF propagates away from the injection borehole, the loading platens can also be expected to affect the propagating fracture. These factors can contribute to HF becoming complex and may result in a combination of different fracturing mechanisms as the perimeter of the HF increases. The tensile events remained much more dominant

for the oil experiments compared to the water experiments, which can point towards a more complex fracture network for water, consisting of a diverse type of fracturing mechanisms. To corroborate this observation, specimens from the oil and water experiments were cut perpendicular to the borehole axis to observe the fractures after the HF experiments. Figure 16 presents the HF generated for the oil and water experiments along with the determined AE event locations. Zoomed-in segments of the fractures at different distances from the injection borehole are also presented in Fig. 16. For oil experiment, a relatively planar less torturous fracture with a wider aperture was obtained compared to the water experiments. Also, the HF were planar with a wider aperture closer to the injection source for both oil and water. As the perimeter of the HF increases, HF become complex and torturous with more branches.

The b values calculated for the individual phases of both the oil and water experiments were close to or greater than 2 (Table 4 and Fig. 9). Generally, a b value of ~ 2 is obtained from the seismicity induced by the main fracturing portion of the field HF operations (Maxwell et al. 2009a; Downie et al. 2010). Wessels et al. (2011) observed a b value of ~ 2 for seismic events generated as a result of HF in the Barnett shale formation in the Ft. Worth Basin, Midcontinent USA. Eaton et al. (2014) calculated the b value for three dissimilar HF projects (Horn River Basin, Central Alberta, and the Cotton Valley), with different geological settings. The seismic data from the gas fields resulted in b values that varied from 1.63 to 2.61. The b values determined for our experiments were in line with what is expected for HF operations. The b value of HF operations can be different than that encountered for natural earthquake sequences, where a b value close to unity is normally encountered. Schorlemmer et al. (2005) suggested that the b value varies depending on the style of faulting, with the highest b values for normal (tensile) faulting, intermediate values for strike-slip, and the lowest values for thrust-type events. Therefore, HF operations, which can consist of substantial tensile or volumetric components, can result in higher b values for the detected microseismicity. The b values for phase-I of both oil and water experiments were characterized by having larger values relative to the other phases, which points towards the presence of a larger fraction of small magnitude events.

4.3 Implications for Field HF Operations

Lower BPs were obtained for the water experiments (Table 4) similar to the field, where it is expected that HF stimulations with the TPR conditions, utilizing for example CO_2 , will result in relatively lower BPs. This lowering of BP can be attributed to the relatively easy penetration of low-viscosity fluid into the micro-cracks/fractures that were either pre-existing or created due to the fluid pressure

surrounding the injection borehole. The geometry of the generated HF also may be much more complex for low-viscosity TPR relative to high-viscosity VPR. The low-viscosity fluid, relative to higher viscosity fluid, can activate the micro-cracks surrounding the propagating HF and can result in a more three-dimensional tortuous fracture with many secondary branches (Ishida et al. 2016). Cuenot et al. (2008) conducted stimulation tests in 2000 and 2003 at Soultz-sous-Forêts France and Zhao et al. (2014) conducted the same in the Basel EGS project, observed high non-DC component microseismic events close to the injection well. In comparison, the non-DC component of microseismic events detected away from the injection source was negligible, indicating minimum effects from fluid overpressure. Ohtsu (1991) applied MT inversion to determine the source mechanisms of microseismic events detected during a small-scale field HF test with water in an Imaichi underground power plant. While the number of microseismic events analyzed was small, tensile cracks were obtained initially around the weak seams followed by shear cracks. Ishida et al. (2019) and (2021) performed small-scale field experiments using water and low-viscosity CO₂, respectively. For both cases, which can be representative of VPR and TPR conditions, tensile events were encountered initially, closer to the injection source, which were followed by abundant shear events. The early tensile dominance detected in these different studies were similar to what had been observed in the current study and can be attributed to the dilation of areas close to the pressurized section. However, in all of the above studies, as the fracture propagated away from the injection source, shear events were the dominant mode of fracturing. In the current study, while the percentage of shear events increased, the non-DC events with larger volumetric components were still the dominant fracturing mode. This discrepancy between laboratory and field experiments in terms of spatio-temporal evolution of the fracture source mechanisms can be attributed to the following factors:

- First, the material tested in the laboratory is mostly intact without any pre-existing faults/discontinuities. In the field, the rock mass contains numerous fractures of varying scales, which can significantly influence the HF propagation. In other words, the experiments performed in the laboratory with intact material represents pure HF experiments involving only new fractures, whereas in the field, it can be a combination of both HF (new fractures) and hydro-shearing (HS) of pre-existing faults/discontinuities.
- Another factor contributing to the highlighted inconsistency can be related to the scale of the experiments/operations. The finite specimen tested in the laboratory may be able to replicate only the near borehole phenomena. In the field, a major portion of the mapped HF may result

in microseismicity detected during HF propagation and extension, which are away from the injection borehole and after the breakdown of the rock formation. These detected microseismic events may be induced by fracturing occurring not only after the instant injection of pressurized fluid but also due to the fluid permeation in the region surrounding the main HF. This can cause stress perturbations or pore pressure changes and may result in the slipping of pre-existing faults/discontinuities (i.e., shear fractures).

- The low percentage of shear fractures detected in small-scale HF studies can also be attributed to the recording limit of the microseismic or AE recording system in the uncontrolled fracturing phase, which is a major portion of HF propagation especially in the field. This overloading of the AE system can be frequently encountered in laboratory HF experiments (e.g., Hampton et al. 2018; Naoi et al. 2020) or in small-scale field HF studies involving brittle rock masses (Ishida et al. 2019) due to the superimposition of many large AE hits and their reflections or clipping of high amplitude signals, which can result in the loss of a significant amount of microseismic data. The majority of these missing AE events could be shear fractures, as they are the likely fracture mode at the failure point (Hajiabdolmajid et al. 2003; Martin and Chandler 1994).
- The extensive and sensitive AE monitoring from all sides of the specimen in the laboratory is almost never possible in the field. Nolen-Hoeksema and Ruff (2001) pointed out that limited microseismic monitoring from only one vertical monitoring well may be blind to the isotropic component of the MT. This type of monitoring setup might not be able to detect the volumetric portion of fracturing. Also, a significant portion of the deformation occurring during the HF stimulation is aseismic (Goodfellow et al. 2015; Villiger et al. 2020), which is also influenced by the distance of the field seismic recording setup from the propagating HF. These conditions may result in a situation where only the high energy seismic events, resulting from the interaction of propagating fractures and pre-existing faults/discontinuities, are detected by the seismic sensors, whereas the relatively low-energy tensile events are left undetected.

5 Conclusions

This study focused on controlled laboratory HF of true-triaxially loaded granitic rock cubes with high- and low-viscosity fluids. The selection of high- (gear oil) and low-viscosity (water) fluids resulted in two different HF propagation

regimes: viscosity-dominated and toughness-dominated, which are accepted as representative of different HF conditions in the field. Utilizing real-time AE monitoring, we successfully mapped the generated fractures by capturing both the fracture initiation and its propagation until the fracture reached the specimen boundaries. The main conclusions are as follows:

- The oil experiments were characterized by higher BPs and injected volume to fracture the rock. Also, the number of AE events, event rates, and event magnitudes was greater for the oil experiments. The low viscosity of water assisted in the relatively easier fluid permeation in the region surrounding the injection borehole and resulted in early breakdown of the specimen utilizing a lower volume of the fluid.
- The geometry of the generated HF was different between the two propagation regimes. For oil, a bi-wing fracture propagated concentrically on either side of the injection point. For water, the fracture propagated randomly on either side of the pressurized section and more towards one direction of the pressurized section.
- The b values of the frequency–magnitude distribution for both the oil and water experiments (~ 2) was similar to those encountered for field HF operations. These b values were higher than those encountered for natural earthquakes (~ 1). For both oil and water, b values for the fracture initiation phases were slightly higher than those of the fracture propagation or post-fracturing phases.
- Tensile fracture mechanisms were dominant for both the oil and water experiments obtained from different source classification procedures. Though, the percentages of tensile fractures were dissimilar for the HF experiments conducted with high- and low-viscosity injection fluids. The experiments conducted with oil were dominated by tensile fracturing events but were not as dominant in the water experiments.
- In the current study, the proportion of source mechanisms were found to vary among the different classification methods and determining the absolute proportions of fracture mechanisms therefore was highly subjective and yielded varying results.

The laboratory experiments, which were conducted using a highly sensitive and extensive microseismic monitoring system, can provide valuable information about HF propagation conducted under different conditions that may not be available in the field. Further experiments with very-high- and very-low-viscosity fluids could enhance our understanding of the ongoing processes.

Acknowledgements This material is based on work supported by the US Department of Energy, Office of Basic Energy Sciences, Geosciences Program under Award No. DE-SC0019117.

Funding This article is funded by Basic Energy Sciences, DE-SC0019117, A. Hedayat.

Data availability The data underlying this article will be shared on reasonable request to the corresponding author.

Declarations

Conflict of interest The authors declare no conflicts of interest relevant to this study.

References

- Aki K (1965) Maximum likelihood estimate of b in the formula $\log N = a - bM$ and its confidence limits. *Bull Earthq Res Inst Tokyo Univ* 43:237–239
- Baig A, Urbancic T (2010) Microseismic moment tensors: a path to understanding frac growth. *Lead Edge* 29(3):320–324
- Bair S (2016) The temperature and pressure dependence of viscosity and volume for two reference liquids. *Lubr Sci* 28(2):81–95
- Bett KE, Cappi JB (1965) Effect of pressure on the viscosity of water. *Nature* 207(4997):620–621
- Bunger AP, Lecampion B (2017) Four critical issues for successful hydraulic fracturing applications. *Rock mechanics and engineering*. <https://doi.org/10.4324/9781315708119-22>
- Bunger AP, Jeffrey RG, Detournay E (2005) Application of scaling laws to laboratory-scale hydraulic fractures. In *Alaska Rocks 2005, The 40th US Symposium on Rock Mechanics (USRMS)*. OnePetro.
- Burridge R, Knopoff L (1964) Body force equivalents for seismic dislocations. *Bull Seismol Soc Am* 54(6A):1875–1888
- Butt A, Hedayat A, Moradian O (2023) Laboratory investigation of hydraulic fracturing in granitic rocks using active and passive seismic monitoring. *Geophys J Int* 234(3):1752–1770
- Cornet FH, Bérard T, Bourouis S (2007) How close to failure is a granite rock mass at a 5 km depth? *Int J Rock Mech Min Sci* 44(1):47–66. <https://doi.org/10.1016/j.ijrmms.2006.04.008>
- Cuenot N, Dorbath C, Dorbath L (2008) Analysis of the microseismicity induced by fluid injections at the EGS site of Soultz-sous-Forêts (Alsace, France): implications for the characterization of the geothermal reservoir properties. *Pure Appl Geophys* 165(5):797–828. <https://doi.org/10.1007/s00024-008-0335-7>
- Dai F, Xia K (2010) Loading rate dependence of tensile strength anisotropy of Barre granite. *Pure Appl Geophys* 167:1419–1432
- Dai F, Xia KW (2013) Laboratory measurements of the rate dependence of the fracture toughness anisotropy of Barre granite. *Int J Rock Mech Min Sci* 60:57–65. <https://doi.org/10.1016/j.ijrmms.2012.12.035>
- Dai F, Xia K, Zuo JP, Zhang R, Xu NW (2013) Static and dynamic flexural strength anisotropy of Barre granite. *Rock Mech Rock Eng* 46(6):1589–1602
- Davidson J, Goebel T, Kwiatek G, Stanchits S, Baró J, Dresen G (2021) What controls the presence and characteristics of aftershocks in rock fracture in the lab? *J Geophys Res: Solid Earth* 126(10):e2021JB022539
- De Pater CJ, Cleary MP, Quinn TS, Barr DT, Johnson DE, Weijers L (1994a) Experimental verification of dimensional analysis for

- hydraulic fracturing. *SPE Prod Facil* 9(04):230–238. <https://doi.org/10.2118/24994-PA>
- De Pater CJ, Weijers L, Savić M, Wolf KHAA, Van Den Hoek PJ, Barr DT (1994b) Experimental study of nonlinear effects in hydraulic fracture propagation (includes associated papers 29225 and 29687). *SPE Prod Facil* 9(04):239–246. <https://doi.org/10.2118/25893-PA>
- Detournay E (2004) Propagation regimes of fluid-driven fractures in impermeable rocks. *Int J Geomech* 4(1):35–45. [https://doi.org/10.1061/\(ASCE\)1532-3641\(2004\)4:1\(35\)](https://doi.org/10.1061/(ASCE)1532-3641(2004)4:1(35))
- Detournay E (2016) Mechanics of hydraulic fractures. *Annu Rev Fluid Mech* 48:311–339. <https://doi.org/10.1146/annurev-fluid-010814-014736>
- Downie RC, Kronenberg E, Maxwell SC (2010). Using microseismic source parameters to evaluate the influence of faults on fracture treatments—a geophysical approach to interpretation. In *SPE Annual Technical Conference and Exhibition*. OnePetro. <https://doi.org/10.2118/134772-MS>
- Eaton DW, Davidsen J, Pedersen PK, Boroumand N (2014) Breakdown of the Gutenberg–Richter relation for microearthquakes induced by hydraulic fracturing: influence of stratabound fractures. *Geophys Prospect* 62(4):806–818. <https://doi.org/10.1111/1365-2478.12128>
- Fallahzadeh SH, Hossain MM, James Cornwell A, Rasouli V (2017) Near wellbore hydraulic fracture propagation from perforations in tight rocks: the roles of fracturing fluid viscosity and injection rate. *Energies* 10(3):359. <https://doi.org/10.3390/en10030359>
- Frohlich C (2001) Display and quantitative assessment of distributions of earthquake focal mechanisms. *Geophys J Int* 144(2):300–308
- Gehne S, Benson PM, Koor N, Dobson KJ, Enfield M, Barber A (2019) Seismo-mechanical response of anisotropic rocks under hydraulic fracture conditions: new experimental insights. *J Geophys Res: Solid Earth* 124(9):9562–9579
- Gischig VS, Doetsch J, Maurer H, Krietsch H, Amann F, Evans KF, Giardini D (2018) On the link between stress field and small-scale hydraulic fracture growth in anisotropic rock derived from microseismicity. *Solid Earth* 9(1):39–61
- Goodfellow SD, Nasserī MHB, Maxwell SC, Young RP (2015) Hydraulic fracture energy budget: insights from the laboratory. *Geophys Res Lett* 42(9):3179–3187. <https://doi.org/10.1002/2015GL063093>
- Grigoli F, Cesca S, Rinaldi AP, Manconi A, Lopez-Comino JA, Clinton JF, Wiemer S (2018) The november 2017 M_w 5.5 Pohang earthquake: a possible case of induced seismicity in South Korea. *Science* 360(6392):1003–1006
- Gulia L, Wiemer S (2019) Real-time discrimination of earthquake foreshocks and aftershocks. *Nature* 574(7777):193–199. <https://doi.org/10.1038/s41586-019-1606-4>
- Gutenberg B, Richter CF (1944) Frequency of earthquakes in California. *Bull Seismol Soc Am* 34(4):185–188
- Hajiabdolmajid V, Kaiser P, Martin CD (2003) Mobilised strength components in brittle failure of rock. *Geotechnique* 53(3):327–336
- Hampton J, Frash L, Gutierrez M (2013) Investigation of laboratory hydraulic fracture source mechanisms using acoustic emission. In *47th US Rock Mechanics/Geomechanics Symposium*. American Rock Mechanics Association.
- Hampton J, Gutierrez M, Matzar L, Hu D, Frash L (2018) Acoustic emission characterization of microcracking in laboratory-scale hydraulic fracturing tests. *J Rock Mech Geotech Eng* 10(5):805–817. <https://doi.org/10.1016/j.jrmge.2018.03.007>
- Hanks TC, Kanamori H (1979) A moment magnitude scale. *J Geophys Res: Solid Earth* 84(B5):2348–2350
- Hedayat A, Pyrak-Nolte LJ, Bobet A (2014) Precursors to the shear failure of rock discontinuities. *Geophys Res Lett* 41(15):5467–5475. <https://doi.org/10.1002/2014GL060848>
- Henley RW, Ellis AJ (1983) Geothermal systems ancient and modern: a geochemical review. *Earth Sci Rev* 19(1):1–50
- Herrmann M, Kraft T, Tormann T, Scarabello L, Wiemer S (2019) A consistent high-resolution catalog of induced seismicity in Basel based on matched filter detection and tailored post-processing. *J Geophys Res: Solid Earth* 124(8):8449–8477
- Horálek J, Jechumtálová Z, Dorbath L, Šílený J (2010) Source mechanisms of micro-earthquakes induced in a fluid injection experiment at the HDR site Soultz-sous-Forêts (Alsace) in 2003 and their temporal and spatial variations. *Geophys J Int* 181(3):1547–1565
- Hu L, Ghassemi A, Pritchett J, Garg S (2020) Characterization of laboratory-scale hydraulic fracturing for EGS. *Geothermics* 83:101706
- Huang L, Liu J, Zhang F, Dontsov E, Damjanac B (2019) Exploring the influence of rock inherent heterogeneity and grain size on hydraulic fracturing using discrete element modeling. *Int J Solids Struct* 176:207–220
- Hudson JA, Pearce RG, Rogers RM (1989) Source type plot for inversion of the moment tensor. *J Geophys Res: Solid Earth* 94(B1):765–774
- Inui S, Ishida T, Nagaya Y, Nara Y, Chen Y, Chen Q (2014) AE monitoring of hydraulic fracturing experiments in granite blocks using supercritical CO₂, water and viscous oil. In *48th US Rock Mechanics/Geomechanics Symposium*. OnePetro.
- Ishida T (2001) Acoustic emission monitoring of hydraulic fracturing in laboratory and field. *Constr Build Mater* 15(5–6):283–295. [https://doi.org/10.1016/S0950-0618\(00\)00077-5](https://doi.org/10.1016/S0950-0618(00)00077-5)
- Ishida T, Chen Q, Mizuta Y, Roegiers JC (2004) Influence of fluid viscosity on the hydraulic fracturing mechanism. *J Energy Resour Technol* 126(3):190–200
- Ishida T, Aoyagi K, Niwa T, Chen Y, Murata S, Chen Q, Nakayama Y (2012) Acoustic emission monitoring of hydraulic fracturing laboratory experiment with supercritical and liquid CO₂. *Geophys Res Lett*. <https://doi.org/10.1029/2012GL052788>
- Ishida T, Chen Y, Bennour Z, Yamashita H, Inui S, Nagaya Y, Nagano Y (2016) Features of CO₂ fracturing deduced from acoustic emission and microscopy in laboratory experiments. *J Geophys Res: Solid Earth* 121(11):8080–8098. <https://doi.org/10.1002/2016JB013365>
- Ishida T, Fujito W, Yamashita H, Naoi M, Fujii H, Suzuki K, Matsui H (2019) Crack expansion and fracturing mode of hydraulic refracturing from acoustic emission monitoring in a small-scale field experiment. *Rock Mech Rock Eng* 52(2):543–553. <https://doi.org/10.1007/s00603-018-1697-5>
- Ishida T, Desaki S, Kishimoto Y, Naoi M, Fujii H (2021) Acoustic emission monitoring of hydraulic fracturing using carbon dioxide in a small-scale field experiment. *Int J Rock Mech Min Sci* 141:104712
- Ito T, Igarashi A, Kato H, Ito H, Sano O (2006) Crucial effect of system compliance on the maximum stress estimation in the hydrofracturing method: theoretical considerations and field-test verification. *Earth, Planets Space* 58(8):963–971
- Ito T, Satoh T, Kato H (2010) Deep rock stress measurement by hydraulic fracturing method taking account of system compliance effect. In *ISRM International Symposium on In-Situ Rock Stress*. OnePetro.
- Jung R (2013) EGS—goodbye or back to the future. In *ISRM International Conference for Effective and Sustainable Hydraulic Fracturing*. OnePetro.
- Knopoff L, Randall MJ (1970) The compensated linear-vector dipole: a possible mechanism for deep earthquakes. *J Geophys Res* 75(26):4957–4963
- Kranz RL, Frankel AD, Engelder T, Scholz CH (1979) The permeability of whole and jointed Barre granite. *Int J Rock Mech Min Sci Geomech Abstr* 16(4):225–234

- Kurz JH, Grosse CU, Reinhardt HW (2005) Strategies for reliable automatic onset time picking of acoustic emissions and of ultrasound signals in concrete. *Ultrasonics* 43(7):538–546
- Kwiatak G, Martínez-Garzón P, Bohnhoff M (2016) HybridMT: a MATLAB/shell environment package for seismic moment tensor inversion and refinement. *Seismol Res Lett* 87(4):964–976
- Lecampion B, Desroches J, Jeffrey RG, Bungler AP (2017) Experiments versus theory for the initiation and propagation of radial hydraulic fractures in low-permeability materials. *J Geophys Res: Solid Earth* 122(2):1239–1263. <https://doi.org/10.1002/2016JB013183>
- Lhomme T, Detournay E, Jeffrey RG (2005) Effect of fluid compressibility and borehole on the initiation and propagation of a transverse hydraulic fracture. *Strength, Fract Complex* 3(2–4):149–162
- Li BQ, Einstein HH (2019) Direct and microseismic observations of hydraulic fracturing in Barre granite and Opalinus clayshale. *J Geophys Res: Solid Earth* 124(11):11900–11916. <https://doi.org/10.1029/2019JB018376>
- Li BQ, da Silva BG, Einstein H (2019) Laboratory hydraulic fracturing of granite: acoustic emission observations and interpretation. *Eng Fract Mech* 209:200–220
- Li M, Zhang F, Zhuang L, Zhang X, Ranjith P (2020) Micromechanical analysis of hydraulic fracturing in the toughness-dominated regime: implications to supercritical carbon dioxide fracturing. *Comput Geosci* 24:1815–1831
- Li BQ, Casanova M, Einstein HH (2023) Laboratory study of fracture initiation and propagation in Barre granite under fluid pressure at stress state close to failure. *J Rock Mech Geotech Eng* 15(3):538–550
- Lockner D (1993) The role of acoustic emission in the study of rock fracture. *Int J Rock Mech Min Sci Geomech Abstr* 30(7):883–899. [https://doi.org/10.1016/0148-9062\(93\)90041-B](https://doi.org/10.1016/0148-9062(93)90041-B)
- Maeda N (1985) A method for reading and checking phase times in autoprocesing system of seismic wave data. *Zisin* 38:365–379
- Martin CD, Chandler NA (1994) The progressive fracture of Lac du Bonnet granite. *Int J Rock Mech Min Sci Geomech Abstr* 31(6):643–659
- Martínez-Garzón P, Kwiatak G, Bohnhoff M, Dresen G (2017) Volumetric components in the earthquake source related to fluid injection and stress state. *Geophys Res Lett* 44(2):800–809
- Maxwell SC (2011) What does microseismicity tells us about hydraulic fractures? In SEG Technical Program Expanded Abstracts 2011. Society of Exploration Geophysicists. pp 1565–1569. <https://doi.org/10.1190/1.3627501>
- Maxwell SC, Cipolla C (2011) What does microseismicity tell us about hydraulic fracturing? In SPE Annual Technical Conference and Exhibition. OnePetro. <https://doi.org/10.2118/146932-MS>
- Maxwell SC, Jones M, Parker R, Miong S, Leaney S, Dorval D, Hammermaster K (2009a) Fault activation during hydraulic fracturing. In: SEG Technical Program Expanded Abstracts 2009. Society of Exploration Geophysicists. pp 1552–1556. <https://doi.org/10.1190/1.3255145>
- Maxwell SC, Waltman CK, Warpinski NR, Mayerhofer MJ, Boroumand N (2009b) Imaging seismic deformation induced by hydraulic fracture complexity. *SPE Reserv Eval Eng* 12(01):48–52
- Maxwell S, Goodfellow S, Lee B, Mack M, Young R (2016) Acoustic-emission geomechanics characterization of laboratory hydraulic fracturing. In 2016 SEG International Exposition and Annual Meeting. OnePetro.
- McClure MW (2012) Modeling and characterization of hydraulic stimulation and induced seismicity in geothermal and shale gas reservoirs (Doctoral dissertation). Stanford University.
- McClure MW, Horne RN (2014a) An investigation of stimulation mechanisms in enhanced geothermal systems. *Int J Rock Mech Min Sci* 72:242–260. <https://doi.org/10.1016/j.ijrmmms.2014.07.011>
- McClure MW, Horne RN (2014b) Correlations between formation properties and induced seismicity during high pressure injection into granitic rock. *Eng Geol* 175:74–80. <https://doi.org/10.1016/j.enggeo.2014.03.015>
- Miller JT (2008) Crack coalescence in granite, Master's Thesis, Massachusetts Institute of Technology.
- Nakamura Y, Hiraiwa S, Suzuki F, Matsui M (2016) High-pressure viscosity measurements of polyalphaolefins at elevated temperature. *Tribol Online* 11(2):444–449
- Naoi M, Chen Y, Yamamoto K, Morishige Y, Imakita K, Tsutumi N, Kitamura S (2020) Tensile-dominant fractures observed in hydraulic fracturing laboratory experiment using eagle ford shale. *Geophys J Int* 222(2):769–780. <https://doi.org/10.1093/gji/ggaa183>
- Nasseri MHB, Mohanty B (2008) Fracture toughness anisotropy in granitic rocks. *Int J Rock Mech Min Sci* 45(2):167–193
- Nasseri MHB, Mohanty B, Young RP (2006) Fracture toughness measurements and acoustic emission activity in brittle rocks. *Pure Appl Geophys* 163(5–6):917–945. <https://doi.org/10.1007/s00024-006-0064-8>
- Niu Z, Li BQ, Moradian O (2023) Moment tensor and stress inversion solutions of acoustic emissions during compression and tensile fracturing in crystalline rocks. *J Rock Mech Geotech Eng*. <https://doi.org/10.1016/j.jrmge.2022.12.024>
- Nolen-Hoeksema RC, Ruff LJ (2001) Moment tensor inversion of microseisms from the B-sand propped hydrofracture, M-site. *Colorado Tectonophys* 336(1–4):163–181
- Norbeck JH, McClure MW, Horne RN (2018) Field observations at the Fenton Hill enhanced geothermal system test site support mixed-mechanism stimulation. *Geothermics* 74:135–149. <https://doi.org/10.1016/j.geothermics.2018.03.003>
- Nur A, Simmons G (1969) Stress-induced velocity anisotropy in rock: an experimental study. *J Geophys Res* 74(27):6667–6674
- Ohno K, Ohtsu M (2010) Crack classification in concrete based on acoustic emission. *Constr Build Mater* 24(12):2339–2346
- Ohtsu M (1991) Simplified moment tensor analysis and unified decomposition of acoustic emission source: application to in situ hydrofracturing test. *J Geophys Res: Solid Earth* 96(B4):6211–6221
- Ohtsu M (1995) Acoustic emission theory for moment tensor analysis. *Res Nondestr Eval* 6(3):169–184. <https://doi.org/10.1007/BF01606380>
- Olasolo P, Juárez MC, Morales MP, Liarte IA (2016) Enhanced geothermal systems (EGS): a review. *Renew Sustain Energy Rev* 56:133–144
- Olsson R (1999) An estimation of the maximum *b*-value in the Gutenberg-Richter relation. *J Geodyn* 27(4–5):547–552. [https://doi.org/10.1016/S0264-3707\(98\)00022-2](https://doi.org/10.1016/S0264-3707(98)00022-2)
- Pan PZ, Wu ZH, Yan F, Ji WW, Miao ST, Wang Z (2020) Effect of the intermediate principal stress on hydraulic fracturing in granite: an experimental study. *Environ Earth Sci* 79(1):10. <https://doi.org/10.1007/s12665-019-8760-8>
- Rydelek PA, Sacks IS (1989) Testing the completeness of earthquake catalogues and the hypothesis of self-similarity. *Nature* 337(6204):251–253. <https://doi.org/10.1038/337251a0>
- Sano O, Kudo Y, Mizuta Y (1992) Experimental determination of elastic constants of Oshima granite, Barre granite, and Chelmsford granite. *J Geophys Res: Solid Earth* 97(B3):3367–3379. <https://doi.org/10.1029/91JB02934>
- Sarmadivaleh M (2012). Experimental and numerical study of interaction of a pre-existing natural interface and an induced hydraulic fracture (Doctoral dissertation, Curtin University).
- Sarmadivaleh M, Joodi B, Nabipour A, Rasouli V (2013) Steps to conducting a valid hydraulic-fracturing laboratory test. *APPEA J* 53(1):347–354. <https://doi.org/10.1071/AJ12029>

- Savic M, Cockram MJ, Ziolkowski AM (1993) Active ultrasonic monitoring of laboratory-scale hydraulic fracturing experiments: numerical modelling vs experiment. In offshore Europe. *Pet Eng*. <https://doi.org/10.2118/26793-MS>
- Savitski AA, Detournay E (2002) Propagation of a fluid-driven penny-shaped fracture in an impermeable rock: asymptotic solutions. *Int J Solids Struct* 39(26):6311–6337. [https://doi.org/10.1016/S0020-7683\(02\)00492-4](https://doi.org/10.1016/S0020-7683(02)00492-4)
- Schmelzer JW, Zanutto ED, Fokin VM (2005) Pressure dependence of viscosity. *J Chem Phys* 122(7):074511
- Schmitt DR, Zoback MD (1992) Diminished pore pressure in low-porosity crystalline rock under tensional failure: apparent strengthening by dilatancy. *J Geophys Res: Solid Earth* 97(B1):273–288
- Schoenball M, Ajo-Franklin JB, Blankenship D, Chai C, Chakravarty A, Dobson P, EGS Collab Team (2020) Creation of a mixed-mode fracture network at mesoscale through hydraulic fracturing and shear stimulation. *J Geophys Res: Solid Earth* 125(12):e2020JB019807
- Schorlemmer D, Wiemer S, Wyss M (2005) Variations in earthquake-size distribution across different stress regimes. *Nature* 437(7058):539–542. <https://doi.org/10.1038/nature04094>
- Selvadurai APS, Boulon MJ, Nguyen TS (2005) The permeability of an intact granite. *Pure Appl Geophys* 162(2):373–407
- Shirole D, Walton G, Hedayat A (2020) Experimental investigation of multi-scale strain-field heterogeneity in rocks. *Int J Rock Mech Min Sci* 127:104212
- Šílený J, Jechumtálová Z, Dorbath C (2014) Small scale earthquake mechanisms induced by fluid injection at the enhanced geothermal system reservoir Soultz (Alsace) in 2003 using alternative source models. *Pure Appl Geophys* 171:2783–2804
- Sleeman R, Van Eck T (1999) Robust automatic P-phase picking: an on-line implementation in the analysis of broadband seismogram recordings. *Phys Earth Planet Inter* 113(1–4):265–275
- Solberg P, Lockner D, Byerlee JD (1980) Hydraulic fracturing in granite under geothermal conditions. *Int J Rock Mech Min Sci Geomech Abstr* 17(1):25–33. [https://doi.org/10.1016/0148-9062\(80\)90003-0](https://doi.org/10.1016/0148-9062(80)90003-0)
- Stanchits S, Surdi A, Gathogo P, Edelman E, Suarez-Rivera R (2014) Onset of hydraulic fracture initiation monitored by acoustic emission and volumetric deformation measurements. *Rock Mech Rock Eng* 47(5):1521–1532. <https://doi.org/10.1007/s00603-014-0584-y>
- Tanaka R, Naoi M, Chen Y, Yamamoto K, Imakita K, Tsutsumi N, Hyodo D (2021) Preparatory acoustic emission activity of hydraulic fracture in granite with various viscous fluids revealed by deep learning technique. *Geophys J Int* 226(1):493–510
- Utsu T (1965) A method for determining the value of "b" in a formula $\log n = a - bM$ showing the magnitude-frequency relation for earthquakes. *Geophys Bull Hokkaido Univ* 13:99–103
- Vavryčuk V (2001) Inversion for parameters of tensile earthquakes. *J Geophys Res: Solid Earth* 106(B8):16339–16355
- Vavryčuk V (2011) Tensile earthquakes: theory, modeling, and inversion. *J Geophys Res: Solid Earth* 116:B12320. <https://doi.org/10.1029/2011JB008770>
- Vavryčuk V (2015) Moment tensor decompositions revisited. *J Seismol* 19:231–252
- Villiger L, Gischig VS, Doetsch J, Krietsch H, Dutler NO, Jalali M, Wiemer S (2020) Influence of reservoir geology on seismic response during decimeter-scale hydraulic stimulations in crystalline rock. *Solid Earth* 11(2):627–655. <https://doi.org/10.5194/se-11-627-2020>
- Warpinski N (2009) Microseismic monitoring: inside and out. *J Petrol Technol* 61(11):80–85. <https://doi.org/10.2118/118537-JPT>
- Warpinski NR, Du J, Zimmer U (2012) Measurements of hydraulic-fracture-induced seismicity in gas shales. *SPE Prod Oper* 27(03):240–252
- Wessels S, Kratz M, De La Pena A (2011) Identifying fault activation during hydraulic stimulation in the Barnett shale: source mechanisms, b values, and energy release analyses of microseismicity. SEG technical program expanded abstracts 2011. Society of Exploration Geophysicists, Houston, pp 1463–1467. <https://doi.org/10.1190/1.3627478>
- Wiemer S, Wyss M (2000) Minimum magnitude of completeness in earthquake catalogs: examples from Alaska, the western United States, and Japan. *Bull Seismol Soc Am* 90(4):859–869. <https://doi.org/10.1785/0119990114>
- Woessner J, Wiemer S (2005) Assessing the quality of earthquake catalogues: Estimating the magnitude of completeness and its uncertainty. *Bull Seismol Soc Am* 95(2):684–698. <https://doi.org/10.1785/0120040007>
- Wu R, Selvadurai PA, Chen C, Moradian O (2021) Revisiting piezoelectric sensor calibration methods using elastodynamic body waves. *J Nondestruct Eval* 40(3):1–19
- Xia K, Nasser MHB, Mohanty B, Lu F, Chen R, Luo SN (2008) Effects of microstructures on dynamic compression of Barre granite. *Int J Rock Mech Min Sci* 45(6):879–887
- Xie L, Min KB, Song Y (2015) Observations of hydraulic stimulations in seven enhanced geothermal system projects. *Renew Energy* 79:56–65. <https://doi.org/10.1016/j.renene.2014.07.044>
- Zafar S, Hedayat A, Moradian O (2022) Evolution of tensile and shear cracking in crystalline rocks under compression. *Theoret Appl Fract Mech* 118:103254
- Zang A, Christian Wagner F, Stanchits S, Dresen G, Andresen R, Haidekker MA (1998) Source analysis of acoustic emissions in Aue granite cores under symmetric and asymmetric compressive loads. *Geophys J Int* 135(3):1113–1130. <https://doi.org/10.1046/j.1365-246X.1998.00706.x>
- Zhao P, Kühn D, Oye V, Cesca S (2014) Evidence for tensile faulting deduced from full waveform moment tensor inversion during the stimulation of the Basel enhanced geothermal system. *Geothermics* 52:74–83. <https://doi.org/10.1016/j.geothermics.2014.01.003>
- Zhuang L, Kim KY, Jung SG, Diaz M, Min KB (2019a) Effect of water infiltration, injection rate and anisotropy on hydraulic fracturing behavior of granite. *Rock Mech Rock Eng* 52(2):575–589. <https://doi.org/10.1007/s00603-018-1431-3>
- Zhuang L, Kim KY, Jung SG, Diaz M, Min KB, Zang A et al (2019b) Cyclic hydraulic fracturing of pocheon granite cores and its impact on breakdown pressure, acoustic emission amplitudes and injectivity. *Int J Rock Mech Min Sci* 122:104065. <https://doi.org/10.1016/j.ijrmms.2019.104065>

Publisher's Note Springer Nature remains neutral with regard to jurisdictional claims in published maps and institutional affiliations.

Springer Nature or its licensor (e.g. a society or other partner) holds exclusive rights to this article under a publishing agreement with the author(s) or other rightsholder(s); author self-archiving of the accepted manuscript version of this article is solely governed by the terms of such publishing agreement and applicable law.